Evolution of flow reversal and flow heterogeneities in high elasticity wormlike micelles (WLMs) with a yield stress

Patrick J. McCauley,[1] Christine Huang,[2] Lionel Porcar,[3] Satish Kumar,[1] and Michelle A. Calabrese[1,a)]

[1]*Department of Chemical Engineering and Materials Science, University of Minnesota, Twin Cities, Minneapolis, Minnesota 55455*
[2]*Department of Materials Science and Engineering, University of Pennsylvania, Philadelphia, Pennsylvania 19104*
[3]*Large Scale Structures, Institut Laue-Langevin, BP 156, F38042 Grenoble Cedex 9, France*

(Received 22 July 2022; final revision received 27 February 2023; published 21 March 2023)

Abstract

The formation and evolution of a heterogeneous flow and flow reversal are examined in highly elastic, gel-like wormlike micelles (WLMs) formed from an amphiphilic triblock poloxamer P234 in 2M NaCl. A combination of linear viscoelastic, steady shear, and creep rheology demonstrate that these WLMs have a yield stress and exhibit viscoelastic aging, similar to some soft glassy materials. Nonlinear shear rheology and rheoparticle tracking velocimetry reveal that these poloxamer WLMs undergo a period of strong elastic recoil and flow reversal after the onset of shear startup. As flow reversal subsides, a fluidized high shear rate region and a nearly immobile low shear rate region of fluid form, accompanied by wall slip and elastic instabilities. The features of this flow heterogeneity are reminiscent of those for aging yield stress fluids, where the heterogeneous flow forms during the initial stress overshoot and is sensitive to the inherent stress gradient of the flow geometry. Additionally, macroscopic bands that form transiently above a critical shear rate become "trapped" due to viscoelastic aging in the nearly immobile region. This early onset of the heterogeneous flow during the rapidly decreasing portion of the stress overshoot differs from that typically observed in shear banding WLMs and is proposed to be necessary for observing significant flow reversal. Exploring the early-time, transient behavior of this WLM gel with rheology similar to both WLM solutions and soft glassy materials provides new insights into spatially heterogeneous flows in both of these complex fluids. © *2023 The Society of Rheology.*
https://doi.org/10.1122/8.0000535

I. INTRODUCTION

Wormlike micelles (WLMs) self-assemble from amphiphilic surfactants and polymers, forming elongated, entangled structures that dynamically rearrange. Depending on the surfactant type, concentration, and temperature, WLMs can behave as viscoelastic solutions or gel-like materials with an apparent yield stress [1–4]. This wide range of WLM stimuli-responsive microstructures and dynamics is ideal for use in cosmetic and drag-reduction applications [5,6] and as model systems for studying nonlinear flow phenomena and flow instabilities [7–9]. A unique flow phenomenon exhibited by WLMs is the formation of shear bands, macroscopic regions of fluid with distinct shear rate, viscosity, and structure. In WLMs, shear band formation is often attributed to a constitutive instability that arises due to a nonmonotonic constitutive relationship [10,11], but can also result from edge fracture [12,13] or flow-concentration coupling [14,15]. Yield stress fluids (YSFs) can also exhibit shear banding due to a nonmonotonic constitutive relationship [16,17] or may form shear bands transiently in fluids with a monotonic constitutive relationship, arising from a stress overshoot [18]. Transient shear banding can persist for long durations [19], but unlike true steady state banding, the homogeneous flow is eventually recovered. However, in some yield stress fluids, transient shear banding can become permanently trapped due to viscoelastic aging, presenting as steady state shear bands [20,21].

The formation of shear bands and other spatially dependent flow phenomena in WLMs following the startup of steady shear has been well-characterized experimentally via techniques that can resolve the flow in both space and time, like rheoparticle tracking velocimetry (rheo-PTV) [11,22–24] or flow-small angle neutron scattering (flow-SANS) [25–28]. For WLMs exhibiting canonical shear banding due to constitutive instability, the WLMs deform elastically at early times in the flow startup: The stress increases linearly with time and the underlying velocity profile is linear. After a few units of strain ($\gamma \approx 2$–6) [29], the stress achieves a maximum and begins rapidly decreasing, a sequence often referred to as the stress overshoot [30]. As the stress decreases, the linear velocity profile destabilizes and becomes dramatically nonlinear [22], with the shear rate varying radially throughout the flow region. This nonlinear flow eventually develops into regions with distinct shear rates; the interface between the shear bands diffuses slowly afterward toward its equilibrium position over long time scales, ten to one hundred times greater than the WLM relaxation time [31].

While many WLM solutions exhibit two macroscopic shear bands due to an underlying constitutive instability, a range of other flow heterogeneities and instabilities may occur in WLMs and yield stress fluids due to inherent

a)Author to whom correspondence should be addressed; electronic mail: mcalab@umn.edu

elasticity. For example, the transient shear bands in Herschel–Bulkley fluids like Carbopol microgels are thought to nucleate from a thin lubrication layer formed at the geometry inner wall following a period of elastic loading and sample failure [19,32]. Additionally, shear banded flows with three regions of distinct shear rates have been reported in both WLMs and YSFs [7,33–35]. In WLMs, these three banded structures have been proposed to arise from microstructural differences near the solid boundaries—suggested in computational studies simulating various boundary conditions [36]—or to arise from interplay with elastic instabilities [37,38]. Shear-banded flows of WLMs are often accompanied by elastic instabilities, generating 2D or 3D secondary flows that may be relatively stationary or spatiotemporally complex [24,39–41]. WLMs with high elasticity may also develop elastic turbulence, highly irregular, multidimensional flow accompanied by large stress fluctuations that interfere with shear banding [42,43]. Recently, Mohammadigoushki *et al.* [44] showed that high-elasticity number (*El*) WLMs undergo transient flow reversal during the flow destabilization period following the stress overshoot. Here, portions of the bulk fluid attain velocities that are in the opposite direction of the imposed wall velocity. Flow reversal resulting from strong elastic recoil has been observed in a variety of other complex fluids like polymer solutions [45,46] and yield stress fluids like polymer gels [30,47].

While clear evidence of flow reversal was only recently observed in WLMs [44,48,49], this phenomenon was anticipated for some time. Strong elastic recoil and flow reversal have been predicted in shear banding WLMs from rheological models like the Vasquez–Cook–McKinley (VCM) and Germann–Cook–Beris (GCB) models that produce a nonmonotonic constitutive relationship by incorporating WLM breakage [50–52]. In these models, the onset of elastic recoil corresponds with rapid breakage of the micelles. This elastic recoil leads to flow reversal that precedes shear banding in most cases, except when suppressed by inertial effects at low elasticity numbers ($El \sim 100$) [50]. Experimentally, studies on numerous formulations of CTAB/NaSal WLMs have found that flow reversal depends on *El*, entanglement density *Z*, and ramp up rate, i.e., the rate at which the shear rate increases from rest [48,49]. These studies suggest that a critical elasticity number $El_c \approx 10^5 - 10^6$ is required for flow reversal of moderately and highly entangled CTAB/NaSal WLMs. Additionally, the presence and strength of flow reversal were linked to the width of the flow curve stress plateau, modulated by the entanglement density *Z*, with stronger (greater negative velocity) flow reversal associated with a wider stress plateau.

A subset of these highly elastic WLMs that may be anticipated to exhibit flow reversal are classified as wormlike micelle gels, which are not true physical gels but exhibit gel-like rheological behavior. Raghavan and Feng [1] defined WLM gels by behaviors exhibited in linear viscoelastic rheological measurements, where a WLM gel exhibits a plateau in G' at low frequencies ($\omega \leq 0.1\,\mathrm{rad}\cdot\mathrm{s}^{-1}$); here, $G' > G''$ by a factor of 10 or more. The most commonly studied WLM gels are formed from zwitterionic surfactants and display a plateau in G' down to at least $\omega = 0.01\,\mathrm{rad}\cdot\mathrm{s}^{-1}$ [2–4]. Most notably, when the apparent viscosity is measured versus shear stress or shear rate, a WLM gel shows an apparent yield stress. In contrast, typical viscoelastic WLMs have a Maxwellian, single relaxation time frequency response and finite zero-shear viscosity. Zwitterionic surfactant solutions may exhibit both viscoelastic and gel-like behavior, typically modulated by temperature [1,2,53]. The relaxation spectrum changes as the solution transitions from a Maxwellian, viscoelastic to gel-like response. However, the plateau moduli often remain similar, suggesting similar microstructures across the transition, which has been confirmed via TEM [1,53]. The gel-like behavior of these WLMs is thought to arise from topological constraints due to large persistence or contour lengths or slow breakage and recombination rates [1].

The high elasticity and yield stress of WLM gels potentially impact the mechanism of stress dissipation in startup flows. Substantial flow reversal—of greater magnitude than that observed in WLMs—has been reported in startup flows of elastic polymer microgels [19,30,47], which are yield stress fluids that also form heterogeneous flows. In Carbopol polymer microgels, shear bands were shown to be transient, eventually giving way to the homogeneous flow [19]. Additionally, the formation of shear bands was preceded by adhesive failure near the moving wall of the flow geometry. Although the high *El* WLMs studied by Rassolov and Mohammadigoushki [48] primarily formed shear bands, these WLMs also exhibited signatures of fluid fracture, characterized by large discontinuities in the velocity profile and regions of plug-like flow. Shear band formation – like that observed in viscoelastic WLMs – and localized sample fracture – like in polymer microgels – have both been suggested in WLM gels [3,4]. However, the rheological signatures associated with both phenomena, such as the stress overshoot and subsequent rapid drop in stress in startup, can appear similar. Unfortunately, direct evidence of the evolution of the local flow field and microstructure to distinguish between these phenomena in WLM gels is lacking.

To address this gap, the formation and evolution of flow reversal and flow heterogeneities are characterized in a new WLM gel formed from nonionic block polymers. Poloxamers are commonly studied block polymer surfactants composed of two hydrophilic polyethylene oxide endblocks (PEO) and a hydrophobic polypropylene oxide (PPO) midblock, which have exhibited WLM shear banding in prior work [7,34]. The dynamics of poloxamer WLMs are far slower than typical small-molecule surfactant WLMs, with solution relaxation times on order 10–1000 s [54] compared to ~1 s relaxation times of systems like CPyCl/Sal WLMs [29,31]. The upper end of the poloxamer relaxation times is more comparable with long-tail surfactant WLM gels with relaxation times $\tau \sim O(10^3)$– $O(10^5)$ s [3,4], suggesting that these systems may be good candidates for forming WLM gels to investigate their flow behavior.

In this article, in-depth flow characterization of a WLM gel is performed for the first time using a combination of shear rheology and rheo-particle-tracking velocimetry (rheo-PTV). This characterization focuses on the transient flow behavior, as the fluid responds to shear start up and

develops distinct heterogeneous regions. Linear rheology and small-angle neutron scattering (SANS) reveal that the poloxamer solution in this work not only has a yield stress, but also exhibits viscoelastic aging, which impacts the observed flow heterogeneities. Rheo-PTV measurements show that the formation of flow heterogeneities in startup flows is accompanied by a wealth of complex flow behaviors including strong elastic recoil and flow reversal, wall slip, and elastic instabilities. The kinematics of flow heterogeneity formation and evolution are found to exhibit characteristics of both viscoelastic WLM solutions and aging yield stress fluids, revealing fundamental insights about the nonlinear flow behavior in both classes of materials.

II. MATERIALS AND METHODS

A. Materials

Poloxamer 234 (P234), also known by the tradename Pluronic P84, was obtained from BASF and used as received. The first two digits in P234 correspond to the PPO block molecular weight and the final digit to the PEO weight fraction, i.e., P234 has a PPO block of ~2.3 kg/mol and is 40% wt PEO. Model P234 solutions were formed at 15% wt in 2M sodium chloride (NaCl), chosen based on prior work reporting shear banding phenomena in 4% wt P234 solutions in 2M NaCl [7,55]. Our prior work confirmed WLM formation and elongation at 4% wt P234 from 0 to 2M NaCl in D_2O [54]; based on this work and the work of others [56–58], these WLMs are unlikely to be branched (see SI.3 for details) [59]. To ensure consistency across small-angle neutron scattering and rheology measurements, D_2O (99.9% mol D, Sigma-Aldrich) was the solvent in all cases, as isotopic substitution often alters the WLM structure and rheology [60]. Sodium chloride (NaCl) was obtained from Fischer Scientific and used as received. To prepare WLM samples, NaCl was first added to D_2O and stirred until well-dissolved. Poloxamer was then added and stirred continuously at 4 °C until the poloxamer fully dissolved and for at least 12 h. All measurements were performed at 38.5 °C except for SANS measurements, which were performed at 39 °C. This small temperature difference accelerates aging (Fig. S1) [59] but does not significantly change the local WLM microstructure, as shown in our prior work [54].

B. Shear rheology

Linear viscoelastic (LVE) rheology and nonlinear controlled stress and shear rate measurements were performed on an Anton Paar MCR 302 stress-controlled rheometer. The geometry, also used for particle tracking velocimetry measurements, is a specialized black anodized aluminum bob of radius $R_i = 16.35$ mm and length $L = 16.5$ mm moving in a transparent cylindrical quartz cell of radius $R_0 = 17.5$ mm (gap-to-radius ratio $\varepsilon = 0.07$ and aspect ratio $\Gamma = L/(R_o - R_i) = 14.35$). Notably, the flow curves obtained in the rheo-PTV geometry are not viscometric flows due to the low aspect ratio, where end effects may be prevalent in viscoelastic WLM solutions [61,62]. However, these effects are expected to be most prominent for very short aspect ratios ($\Gamma < 4$) [61] and flow curves generated in other geometries with higher Γ show similar behavior to that generated in the rheo-PTV geometry; see Fig. S2 [59]. Circulating fluid at a desired temperature flows around the outer cylinder. Evaporation was mitigated in all measurements using a solvent trap.

The rheology of poloxamer WLMs can depend on deformation and thermal history [54,63,64]; therefore, a protocol with consistent shear and thermal treatment was applied before each measurement to rejuvenate the sample. Poloxamer micelles transition from spherical to cylindrical morphologies above a sphere-to-rod transition temperature [65]. Micelle elongation and WLM formation are promoted with increasing temperature beyond this transition [54]. Therefore, before each measurement, the sample was rejuvenated by cooling via a separate chiller operating set to 20 °C, well below the temperature where WLMs are stable [54]. The sample was sheared continuously $\dot{\gamma} = 1\,s^{-1}$ at 20 °C for 5 min to destroy any lingering structure. A final 5 min rest period at 20 °C was imposed before reattaching the flow cell to the heat bath (38.5 ± 0.1 °C) to heat the sample to above the sphere-to-rod transition (32.5 °C for 4% wt P234 in 2M NaCl) [54].

The formation and growth of WLMs at 38.5 °C were monitored via small-amplitude oscillatory shear (SAOS) at a strain amplitude and frequency of $\gamma_0 = 1\%$ and $\omega = 1$ rad·s^{-1}, respectively. The dynamic moduli were found to evolve over long times, a signature of viscoelastic aging [66,67] exhibited by this system (see III A). Therefore, the rheology depends on the wait time t_w prior to the measurement. All nonlinear rheologies were performed after $t_w \approx 30$ min. The time is approximate because, in practice, the sample was aged until the storage modulus $G' = 24$ Pa using the aforementioned SAOS protocol, as slight variations upon loading or rejuvenation can alter the aging process. The wait time to achieve this G' did not vary more than ±1 min. Brief frequency sweeps between tests ($\gamma_0 = 1\%$, $\omega = 1 - 10\,\text{rad}\cdot\text{s}^{-1}$) yielded identical results, confirming the same structure is obtained in the aging process and evaporation did not irreversibly alter the sample composition.

The stress versus shear rate flow curve was measured using a combination of controlled stress (creep) and controlled shear rate measurements. Creep measurements provide better accuracy and less noise at low shear rates than controlled shear rate measurements on stress-controlled rheometers. The strain response was measured over a range of applied stresses ($\sigma = 0.1$–15 Pa) to fully characterize the low shear rate region of the flow curve. Startup protocols were used at high shear rates ($\dot{\gamma} = 0.02$–2 s^{-1}), where startup is defined as a step increase to an applied shear rate $\dot{\gamma}$ from rest. The ramp-up time to the desired shear rate of <0.1 s was significantly faster than the system dynamics. The impact of varying ramp-up time was not explored. Ramp-down protocols, where the shear rate is incrementally stepped down, were performed to access intermediate to low shear rates ($\dot{\gamma} = 0.02$–0.0005 s^{-1}). The stress response was measured for 2 h in startup measurements (or until significant secondary flows and air entrainment were detected, see Fig. S3 [59]) and 2–3 h in ramp-down measurements, where longer measurements are taken at lower shear rates.

C. Rheo-particle tracking velocimetry

Simultaneous rheology and local velocity measurements were performed using well-established rheo-particle tracking velocimetry instrumentation [11,22]. Rheo-PTV experiments were performed using the same anodized aluminum bob and transparent quartz cell geometry used for LVE and flow curve measurements. The quartz cell is illuminated with a 0.3 mm laser light sheet (60–150 mW CNI 532 nm low noise laser). Light is scattered from tracer particles (200 ppm 8–12 μm TSI Hollow-glass spheres) added to the sample, which were verified not to significantly affect the rheology.

Prior to the measurement, samples were sonicated to disperse the particles for at least 5 min and loaded into the geometry at room temperature; care was taken to remove bubbles before and after sample loading. The sample was then heated to the measurement temperature of 38.5 °C in the geometry. The rejuvenation protocol for rheo-PTV measurements during shear startup is identical to that described for shear rheology without PTV. An identical $t_w = 30$ min wait time at 38.5 °C was applied before each measurement.

Particle positions during startup were recorded using a Lucam Lm165 CCD camera, and particle trajectories were identified using the open-source package TrackPy [68] that extends the widely used tracking algorithm of Crocker and Grier [69]. Velocity profiles throughout startup are typically averaged over 1–4 s intervals, corresponding to ~25–100 frames, where shorter intervals better capture the evolving dynamics at earlier times. The velocity is expected to be approximately constant within this averaging interval as the length of time is small compared to the time scale of the flow. The radial position in the gap is reported relative to the inner cylinder such that the normalized gap position $r/H = 0$ at the inner cylinder and $r/H = 1$ at the outer cylinder. Uncertainty is estimated from the root-mean-square deviation of the predicted trajectory with velocity v_{avg} from the measured particle trajectory.

D. Small-angle neutron scattering

SANS was conducted at the Institut Laue Langevin on the D-22 SANS instrument; the dataset is included in Ref. 70. Sample-to-detector distances (SDD) of 11.2 m (11.2 m detector distance and 40 mm diameter source aperture collimation), 5.6 m (5.6 m detector distance and 40 mm diameter source aperture collimation), and 1.3 m (1.3 m detector distance and 40 mm diameter source aperture collimation), a neutron wavelength of $\lambda = 5$ Å, and a wavelength spread of $\Delta\lambda/\lambda = 10\%$ were used to give a scattering vector range of $0.004 < q < 0.6\,\text{Å}^{-1}$. Samples were rejuvenated between trials by cooling to 5 °C for 5–10 min. This protocol was verified via scattering from the sample during this cooling period. Data were analyzed and reduced to an absolute scale, independent of the instrument parameters, using the ILL Grasp software, version 7.14.

Reduced one-dimensional SANS intensities were fit using a cylinder form factor $P(q)$ from the Pedersen model for block polymer micelles [71–73] and are described in-depth in our previous publication [54]. Briefly, to minimize overfitting, known parameters were fixed and used to constrain parameter ranges when applicable: poloxamer concentration, instrument q resolution, solvent and poloxamer scattering length densities, and poloxamer block volumes. Four parameters are fit for WLMs, assuming a solvent-free core: core radius R_c, corona chain radius of gyration R_g, core radii polydispersity σ, and contour length L (Table S1 [59]). Note however, given the concentration of these solutions, intermicelle scattering at higher length scales prevents accurate determination of the micelle length L. Therefore, the fitting region is truncated to only include $q > 0.035\,\text{Å}^{-1}$ as done in the previous work [54].

III. RESULTS

A. Wormlike micelle structure and properties via linear rheology and SANS

Continuous small amplitude oscillatory shear (SAOS) following a step change in temperature (20–38.5 °C) reveals the dynamic moduli of 15% wt P234 solutions increase by orders of magnitude, characteristic of a transition from spherical micelles to elongated wormlike micelles [54] [Fig. 1(a)]. Following the initial rapid increase in both moduli, the storage modulus G' increases logarithmically with time, whereas the loss modulus G'' achieves a maximum near when the moduli intersect ($t = 730$ s) and subsequently decreases. The rate of change of both moduli slows as time progresses, though no steady state response is reached after 1 h of measurement. This behavior is a signature of viscoelastic aging [66,67], structural evolution that becomes more sluggish with time leading to progressively longer relaxation dynamics.

Due to the aging process, the linear and nonlinear rheologies of P234 WLMs depend on the wait time t_w prior to starting a measurement. Increasing the wait time before performing frequency sweeps increases G' and reduces G'' at all measured frequencies [Fig. 1(b)]. Note that the frequency response evolves during the measurement because of aging and the finite time required to measure each data point. Each data point in the frequency sweep is time-dependent and, therefore, in each trial, the same frequencies are applied in the same order (increasing frequency) for accurate comparison. The largest difference in moduli is observed at the lowest, and first, frequency measured $\omega = 0.01$ rad/s. The moduli are closer in value at high frequencies, the last measured, as a result of aging that occurs during measurement.

Time-dependent frequency sweeps reveal that aging is related to an increasing entanglement density. The average entanglement density $\langle Z \rangle$ is estimated from the ratio of the dynamic moduli at the frequency where G'' is a local minimum [74]: $G'_{\text{min}}/G''_{\text{min}} \approx 0.317\langle Z \rangle^{0.82}$. Note this correlation does not consider the effects of micelle branching, but branching is not likely in these nonionic WLMs (SI.3 [59]). Additionally, this correlation was derived from experiments on canonical viscoelastic WLMs and, therefore, the $\langle Z \rangle$ estimated for these gel-like WLMs with a yield stress and aging may not be exact. Using this correlation and the data in Fig. 1, the entanglement density is estimated to be $\langle Z \rangle = 164$, 200, and 228 for wait times of $t_w = 30$, 45, and 60 min, respectively. The increase in $\langle Z \rangle$ could be attributed

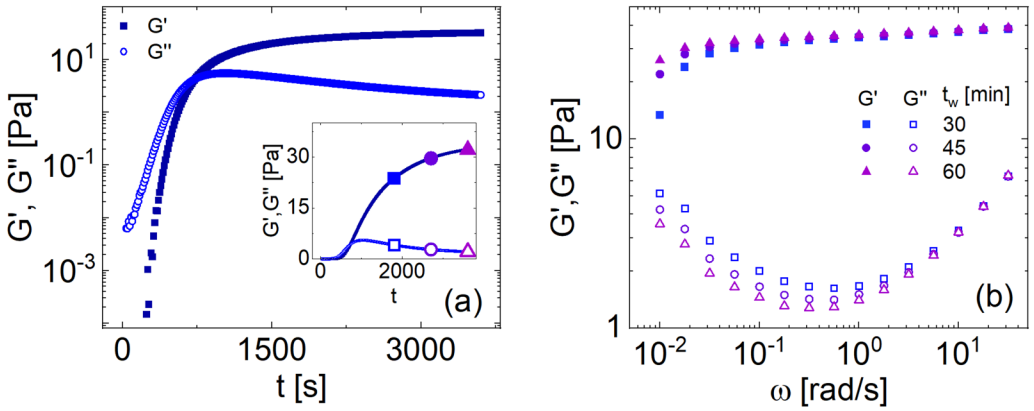

FIG. 1. Small amplitude oscillatory shear ($\gamma_0 = 1\%$) of 15% wt P234 in 2M NaCl/D_2O at 38.5 °C. (a) Evolution of G' and G'' following a step change in temperature (20 °C → 38.5 °C, $\omega = 1$ rad·s^{-1}); the inset shows G' and G'' on a linear scale. Frequency sweeps (b) show an increase in G' and decrease in G'' as wait time t_w prior to measurement increases, attributed to a slow growth of the average micelle contour length.

to an increase in $\langle L \rangle$ or a decrease in the entanglement length l_e as $\langle Z \rangle = \langle L \rangle / l_e$. Estimates of both parameters suggest that an increase in $\langle L \rangle$ is the dominant contribution to $\langle Z \rangle$; see details in SI.6 and summarized values in Table S2 [59].

Static small angle neutron scattering (SANS) (Fig. 2) provides additional evidence for WLM formation and aging resulting from changes in micelle contour length. The scattering intensity increases with wait time up until ~14 min, after which the intensity is time-invariant in the measured q-range [$0.004 < q < 0.066$ Å, Fig. 2(a)]. The scattering becomes time-invariant after a wait time similar to when the dynamic moduli cross over and $G' > G''$, suggesting that aging beyond this time is a result of structural evolution on length scales larger than those accessible in this q-range. As the contour length is beyond the SANS-accessible length scale, this observation is consistent with the contour length-driven aging suggested by the frequency sweeps.

Although the contour length is inaccessible, fits of scattering intensity to the Pedersen rod model after $t_w > 14$ min [Fig. 2(b)] yield a cross-sectional core radius of $R_c = 38$ Å and total radius $R_t = 56$ Å, in good agreement with prior results on more dilute, 4% wt P234 WLMs [54]. This total radius is larger than in typical surfactant WLMs; for example, the radius of CPyCl/NaSal WLMs is threefold smaller ($R_t \sim 18$ Å) [27,75]. Note fitting using the cylindrical micelle form factor does not capture the scattering at lower q-values. In that region, the form factor $P(q) \sim q^{-1}$, but this scaling is masked by intermicelle interactions due to the high concentration of this solution.

B. Yield stress characterization via shear flow curve

The shear flow curve or the relationship between the shear rate and shear stress (Fig. 3) suggests that these 15% wt P234 WLMs have a yield stress, a feature absent in less concentrated P234 WLMs [7]. Similar to LVE rheology, the measured flow curve depends on the wait time prior to measurement due to continual aging. To limit the scope of this study, here each point on the flow curve was measured after only one wait time, $t_w = 30$ min. As a consequence of the yield stress, the flow curves obtained using controlled stress (creep) versus controlled shear rate protocols differ significantly. Time-dependent controlled shear rate and creep measurements used to construct this flow curve are shown in Figs. S4 and S5 [59], respectively.

The flow curve can be used to quantify two yield stresses, a static and a dynamic yield stress [16,66,76,77]. In creep measurements, the shear rate increases several orders of magnitude from $\dot{\gamma} \approx 10^{-4}$ s^{-1} to above 10^{-1} s^{-1} when applied stress is increased from $\sigma = 12$ Pa to $\sigma = 15$ Pa (Fig. 3, ■).

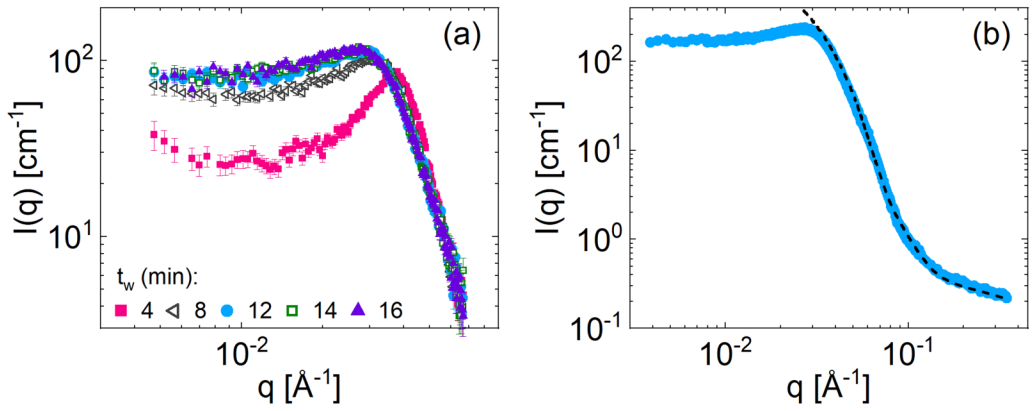

FIG. 2. 1D SANS intensities (a) with increasing wait time t_w and (b) over a broader q-range after a time-invariant scattering intensity is achieved. The dashed line indicates the fit to the Pedersen rod model form factor.

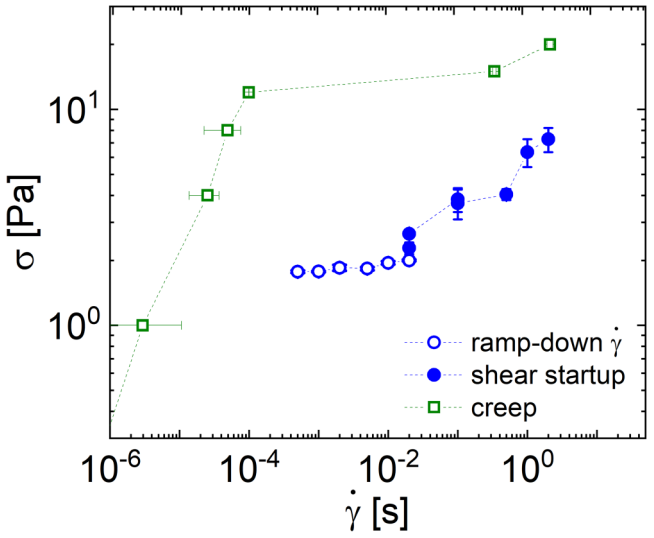

FIG. 3. Flow curve for 15% wt P234 in 2M NaCl/D_2O and a wait time of $t_w = 30$ min, constructed using a combination of creep, ramp-down-shear, and startup-shear protocols. Dashed lines connecting points are included for visual aid. Additional flow curve measurements following the same protocol but acquired using different geometries show similar results; see Fig. S2 [59].

Separating these two regions is some critical stress needed to induce an appreciable flow, known as the static yield stress. However, as shear rate is decreased in controlled shear rate protocols, the stress approaches a much lower value of $\sigma(\dot{\gamma} \to 0) \approx 2$ Pa. This limiting stress value is called the dynamic yield stress, which is the minimum stress required to maintain the flow. The reported flow curve is similar when following the same protocol but measured using different geometries; see Fig. S2 [59]. Supplemental flow curve measurements using ramp-up and ramp-down protocols at 38.5 °C and additional flow curve measurements at 39 °C, a higher temperature that accelerates aging, further validate the importance of aging in this system. The shear rate ramps display hysteresis often observed in thixotropic and viscoelastic aging fluids [78–80], and the dynamic yield stress is higher at 39 °C with an equivalent wait time due to accelerated aging (Fig. S2 [59]).

The measured flow curve values are likely influenced by other complex flow behaviors including wall slip, elastic instabilities, and long transients. Wall slip is a common phenomenon in both WLMs and yield stress fluids and is often significant at low shear rates or in smooth geometries [81,82]. In previously examined, less concentrated P234 WLMs, a region of the flow curve differentiated by significant wall slip was observed at shear rates prior to the onset of shear banding [7]. Here, wall slip likely reduces the stress measured at low shear rates in shear rate-controlled measurements, as occurs in other yield stress fluids [83–85]. This hypothesis is supported by particle tracking velocimetry, which reveals that the onset of significant wall slip coincides with a drop in the measured stress in the startup flow at $\dot{\gamma} = 0.02\ s^{-1}$ (see Sec. III C 2).

Although wall slip is important at low applied shear rates, at higher applied shear rates ($\dot{\gamma} = 1,\ 2\ s^{-1}$), elastic instabilities eventually form, characterized by an increasing stress that fluctuates irregularly (Fig. S4 [59]). This behavior is characteristic of elastic turbulence observed in other WLMs at high shear rates [41–43], including lower concentration P234 WLMs [7]. PTV measurements confirm that complex, 3D flow structures associated with elastic turbulence indeed accompany these large stress fluctuations (see SI.22.4 [59] for video).

Finally, the possibility of long transients, as is often observed in yield stress fluids, must be acknowledged when reporting this flow curve. Although measurements were performed for hours, transient flow states persisting over longer time scales (~10 h) have been reported in yield stress fluids like Carbopol [16,19], where the duration of the transient is greater at lower applied shear rates and applied stresses closer to the static yield stress. Here, the values of stress (controlled shear rate) and shear rate (creep) reported on the flow curve are stable over at least a 30-min duration (Figs. S4 and S5 [59]). However, the possibility remains that these values might change with longer observation time as occurs in Carbopol. Notably, the signatures of this extremely long transient in Carbopol detected via rheology and velocimetry [19,32] are inconsistent with many of the transient properties of this fluid. These rheological and velocimetry features will be compared between fluids in the *Discussion*.

The stability observed over this long time window could instead reflect a yield stress fluid displaying a nonmonotonic constitutive relationship (distinct from the mechanism typically proposed for WLMs) [16,17,86] or could occur due to the viscoelastic aging in the system, as aging effects can extend the lifetime of transient flow states or stabilize them indefinitely [20,21,87]. These possibilities and the proposed fluid classification are detailed further in the *Discussion*. Unfortunately because these systems are aqueous and measurements are performed at elevated temperatures, longer-time measurements cannot be performed accurately due to significant evaporation effects. For these reasons, the reported shear flow curve should be interpreted cautiously.

C. Examining evolution of the heterogeneous flow via shear startup and PTV

For a range of applied shear rates on the flow curve, a heterogeneous flow is observed, with a fluidized region closer to the moving inner cylinder adjacent to a nearly immobile fluid region closer to the stationary outer cylinder. Given that these WLMs share characteristics of both traditional viscoelastic WLMs and yield stress fluids, these distinct regions of heterogeneous flow are occasionally referred to herein as "bands" separated by a band interface; however, these bands are not necessarily formed due to constitutive instability (see *Discussion*). The evolution to this heterogeneous flow state during shear startup can be well-characterized using rheo-PTV. Representative velocity profiles at three shear rates ($\dot{\gamma} = 0.02,\ 0.1,$ and $0.5\ s^{-1}$) as the shear stress evolves with increasing strain reveal unique time-dependent flow behaviors, including flow reversal and development of the band interface (Fig. 4), wall slip, and secondary flows. Note the stresses in PTV trials at lower shear rates approach the steady state stress values of longer startup trials used to

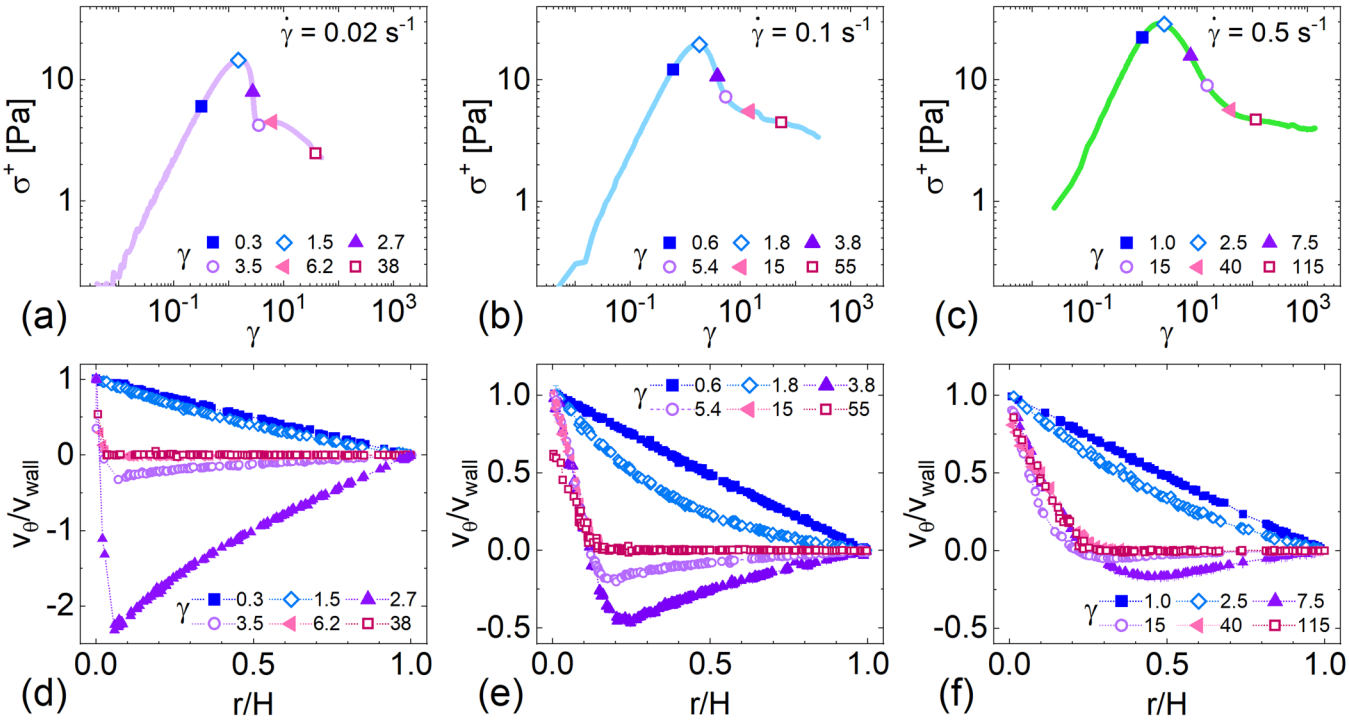

FIG. 4. Shear stress σ versus strain $\gamma = \dot{\gamma}t$ of startup flows with an applied shear rate of $\dot{\gamma} =$ (a) 0.02, (b) 0.1, and (c) 0.5 s^{-1} and corresponding velocity profiles (d)–(f), respectively. Replicate startups for longer acquisition times at $\dot{\gamma} = 0.02$ and 0.1 s^{-1} demonstrate that the stresses in (a) and (b) approach steady values (Fig. S6 [59]). Pronounced elastic recoil leads to negative velocities across the gap immediately following the stress overshoot (▲, ○), the relative magnitude of which decreases with the increasing shear rate.

construct the flow curve (Fig. S6 [59]). Additional PTV measurements at higher shear rates ($\dot{\gamma} = 1$ and 2 s^{-1}) reveal similar flow behaviors (Fig. S7); however, at these higher shear rates, the magnitudes of flow reversal and wall slip are negligible in comparison to those observed at lower shear rates.

Heterogeneous flows can develop in yield stress fluids and WLMs due to edge-induced fracture [48,88,89] or adhesive failure of the sample at a boundary [19,47]. However, the heterogeneous flows observed here are not attributed to these mechanisms, as no evidence of fracture is observed in these startup measurements. For example, no visual indication of air penetrating the measurement gap nor abrupt drop in normal force is observed, the latter of which is a proxy for large changes in the stresses normal to the air-liquid interface. Fracture-induced heterogeneity—which does lead to these distinct visual and rheological signatures—is obtainable in these poloxamer WLMs, but only when the sample has been aged for substantially longer times (see Fig. S9 and associated discussion in SI.10 [59]).

1. Flow reversal following the stress overshoot

The stress and underlying fluid velocity evolve in a similar manner across the three selected shear rates (Fig. 4); however, the magnitudes of specific features are shear rate-dependent. Initially the stress increases with time (or strain) with a linear underlying velocity profile (blue ■, Fig. 4). At a strain of $\gamma \approx 2$, the stress achieves a maximum for all three shear rates, and a weakly shear thinning velocity profile forms (blue ◇). Afterward, the stress rapidly decreases and concurrently a highly nonlinear velocity profile develops, with velocities becoming negative in large portions of the gap (purple ▲, ○). Over time this flow reversal subsides, and two distinct flow regions form in the gap (pink □): a high shear rate, fluidized band near the moving inner wall ($r/H = 0$), and a relatively motionless portion of fluid that extends inward from the stationary outer wall ($r/H = 1$). A video of the early dynamics during startup at $\dot{\gamma} = 0.1\ s^{-1}$ is embedded in SI.22.1 [59].

Comparing the velocity profiles across applied shear rates reveals that the relative magnitude of flow reversal (i.e., the relative magnitude of the negative velocities) is greatest for the lowest shear rate, $\dot{\gamma} = 0.02\ s^{-1}$, and decreases with increasing shear rate (Fig. 4). At the highest measured shear rates ($\dot{\gamma} = 1$ and 2 s^{-1}), flow reversal is barely perceptible in the velocity profiles (Fig. S7 [59]); the absolute magnitude of flow reversal is also smaller than at lower shear rates (Fig. S11 [59]). This finding aligns with prior observations on CTAB/NaSal WLMs by Rassolov and Mohammadigoushki [49], where the relative magnitude of flow reversal was greatest at $Wi = 20$ and weakened with increasing shear rate. Despite a fivefold difference in wall velocity between each shear rate, the minimum velocity in the gap, $v_{min}(t)$, is approximately equal for $\dot{\gamma} = 0.02\ s^{-1}$ and 0.1 s^{-1} and is only twice as large for $\dot{\gamma} = 0.5\ s^{-1}$ [Fig. 5(a)]. With increasing shear rate, flow reversal begins at marginally higher strains and persists over a greater strain width. For example, flow reversal begins at an acquired strain of $\gamma \approx 2.4$ and persists until $\gamma \approx 3.7$ for $\dot{\gamma} = 0.02\ s^{-1}$, whereas the onset of reversal is at $\gamma \approx 4.3$, which persists until $\gamma \approx 24$ for $\dot{\gamma} = 0.5\ s^{-1}$. This observation aligns with the evolution of shear stress,

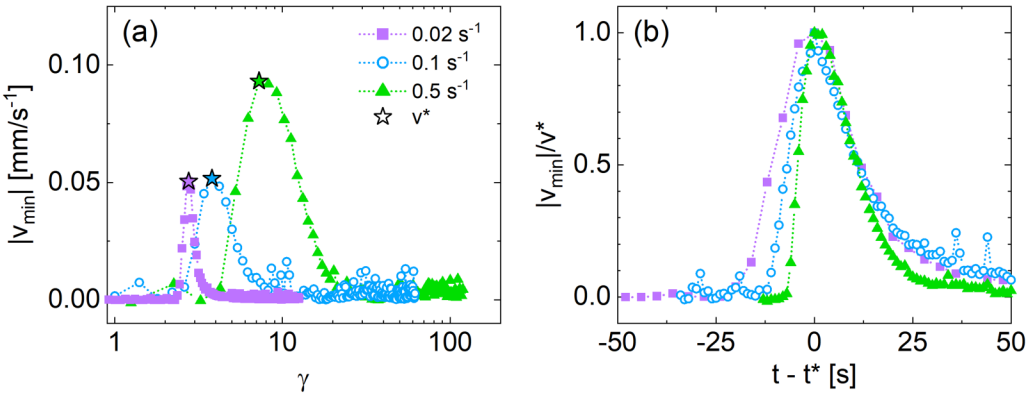

FIG. 5. Magnitude of minimum gap velocity, $|v_{\min}(t)|$, during startup flow: (a) on an absolute scale versus strain; (b) normalized by the magnitude of the global minimum (most negative) velocity during flow reversal, v^*, versus time; here t is shifted by the time at which v^* occurs, t^*. Despite a fivefold difference in magnitude between each $\dot{\gamma}$, the length of time where $v_{\min}$ is significant ($v_{\min}/v^* > 0.1$) varies by no more than twofold across $\dot{\gamma}$.

which decreases more rapidly with strain immediately following the stress overshoot at lower shear rates; see slopes in decreasing σ regions, Figs. 4(a)–4(c).

The increasing strain width of flow reversal with increasing shear rate results from a weak dependence of the flow reversal lifetime on the shear rate, as shown in Fig. 5(b). For facile comparison across shear rate, the minimum velocity in the gap, $v_{\min}(t)$ is normalized by the global minimum reversal velocity (i.e., greatest magnitude negative velocity) throughout startup, v^*, and time is shifted by the time at which v^* occurs, t^*. Remarkably, the time interval of flow reversal Δt_{rev}—defined here as times at which flow reversal is significant ($v_{\min}(t)/v^* > 0.1$)—only decreases slightly with increasing shear rate. For example, despite a 25-fold difference in shear rate, $\Delta t_{rev} = 48\,\text{s}$ at $\dot{\gamma} = 0.02\,\text{s}^{-1}$ versus $\Delta t_{rev} = 30\,\text{s}$ at $\dot{\gamma} = 0.5\,\text{s}^{-1}$. Therefore, while the onset of flow reversal depends on strain (corresponding to the stress overshoot), the evolution of flow reversal is a time-dependent phenomena. Subsequently, the strain interval of flow reversal $\Delta\gamma_{rev} = \dot{\gamma}\Delta t_{rev}$ increases with shear rate, as the reduction in Δt_{rev} is small relative to the change in $\dot{\gamma}$. With further increases in strain (and time), the period of flow reversal ends and the minimum gap velocity is approximately zero for each of the three applied shear rates [Fig. 5(a)], corresponding to a practically motionless fluid region near the outer wall.

In summary, both the lifetime and absolute magnitude of flow reversal depend weakly on shear rate. One contributing factor to the shorter lifetime of flow reversal at higher shear rates is likely the increased velocity of the moving boundary; the negative retraction of fluid due to elastic recoil is in competition with the positive motion of fluid due to momentum transfer from the moving boundary. This reasoning also explains the weaker relative magnitude of flow reversal at higher shear rates seen here and elsewhere [49]. The relative magnitude of flow reversal observed here—more than twice the wall velocity at the lowest shear rate—is the largest magnitude reported in any system to our knowledge and is more consistent with predictions by the VCM or GCB model in the startup flow [50]. This agreement is potentially related to the similarity in when the heterogeneous flow is first observed in this system and in yield stress fluids. The duration of flow reversal is also rationalized by comparing these poloxamer WLMs to YSFs, an idea expanded upon in the *Discussion*.

2. Transient wall slip

Wall slip persists throughout startup for each of the applied shear rates, increasing in magnitude at longer times and larger strains. Figure 6 shows the velocity one particle width (10 μm) from the inner wall with increasing strain for each applied shear rate; the region of flow reversal is indicated by darkened symbols in each dataset. The magnitude of wall slip during flow reversal appears to increase with applied shear rate, where wall slip is essentially absent during flow reversal at $\dot{\gamma} = 0.02\,\text{s}^{-1}$. A greater degree of wall slip during flow reversal is observed at $\dot{\gamma} = 0.5\,\text{s}^{-1}$, up to ~15% of the wall velocity, v_{wall}. However, interestingly, flow reversal occurs whether or not significant (or any) wall slip occurs concomitantly.

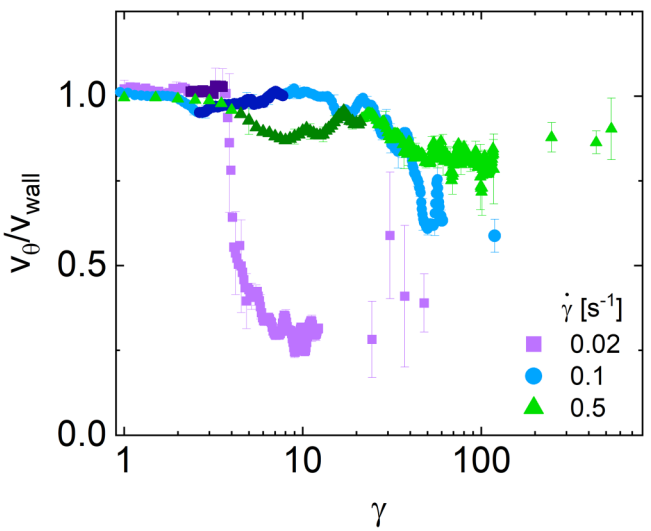

FIG. 6. Velocity of the fluid 10 μm from the inner wall normalized by the imposed wall velocity with increasing strain of three startup flows. Darkened symbols denote the region of flow reversal for each shear rate. Sparse points at large strains result from brief PTV acquisitions at long times. The relative magnitude of wall slip decreases monotonically with shear rate at large strains.

Wall slip increases dramatically at high strains for the lower shear rates; at higher shear rates ($\dot{\gamma} = 1$ and $2\,s^{-1}$), no appreciable wall slip is observed during startup (Fig. S12 [59]). For example, the near-wall velocity drops to almost 30% of v_{wall} for $\dot{\gamma} = 0.02\,s^{-1}$. Furthermore, for $\dot{\gamma} = 0.02$, the onset of substantial wall slip ($\gamma \geq 4$) corresponds to a subsequent local maximum in the stress ($\gamma \approx 6$) after which σ rapidly decreases with time, supporting the hypothesis that wall slip reduces the measured stress at low shear rates. Note that quantifying the degree of wall slip is challenging at low shear rates due to the small width of the high shear rate band and, therefore, the degree of wall slip could be overestimated, considered further in the *Discussion*. The slip velocity also fluctuates in time, a common occurrence in heterogeneous flows of elastic wormlike micelles and yield stress fluids [30,40,90,91].

While flow reversal in this system does not appear to depend on wall slip, an interdependence of wall slip and elastic recoil may be expected in some complex fluids given the large shear rates near the inner wall during elastic recoil and concomitant flow reversal. For example, these two phenomena are directly related in Carbopol microgels exhibiting flow reversal [30]. In these microgels, significant wall slip is documented at the maximum stress in the overshoot region, as the sample begins to fail following a period of elastic loading. A thin lubrication layer following sample failure then leads to total wall slip and flow reversal in the region of rapidly decreasing stress following the overshoot [30]. Wall slip and flow reversal have also been observed in WLMs simultaneously [44,48], where the authors noted that wall slip is maximal around the time of maximum flow reversal and decreases as flow reversal subsides. However, this behavior was not universal in these systems; depending on the solution elasticity number, *El*, slip can instead increase monotonically with strain [48]. The former effect appears significant here for only $\dot{\gamma} = 0.5\,s^{-1}$, whereas the latter mechanism generally describes the three applied shear rates well, as slip increases on average with increasing strain (Fig. 6). Significant wall slip has been observed previously in poloxamer systems, most notably by Manneville and co-workers [7] on a less concentrated, 4% P234 WLMs in 2M NaCl. In that work, significant wall slip was associated with shear banding, with the fluid velocity at the inner wall reducing to 40% of the wall velocity or less at low shear rates.

3. Formation of fluidized and nearly immobile band

Two macroscopic bands form as flow reversal subsides and, therefore, the properties of these two distinct regions—the interface position and local shear rate in the high shear rate and low shear rate regions—evolve to their pseudosteady values during flow reversal. With increasing time, the gap position of minimum velocity $v_{\min}$, $r/H_{v_{\min}}$, approaches the location where the band interface eventually forms, r/H_{int} (Fig. 7); similar behavior is also observed at higher shear rates (Fig. S13 [59]). Before the onset of flow reversal, the minimum velocity is at the stationary outer wall ($r/H = 1$), where the velocity is zero. As time progresses and the flow

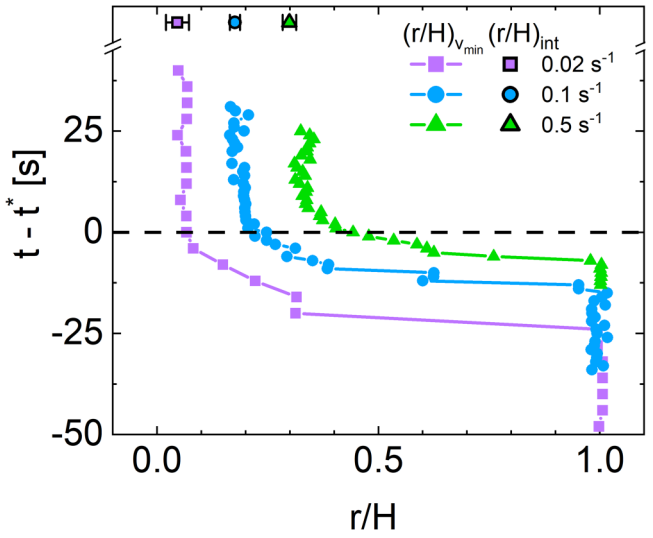

FIG. 7. Gap position r/H of the minimum velocity (closed symbols) and interface between the fluidized and nearly immobile regions (outlined symbols) with increasing time relative to the maximum flow reversal time, t^* in the startup flow. The dotted line denotes $t = t^*$. For open symbols, error bars correspond to undulations in the interface position.

begins to reverse, the position of v_{min} moves quickly through the gap toward the inner wall (solid symbols, Fig. 7). The region of flow reversal does not propagate as close to the inner wall with increasing shear rate; the increased momentum from the faster-moving inner wall at higher shear rates counteracts the retraction of the fluid. Additionally, after the maximum magnitude of flow reversal is achieved ($t - t^* = 0$), the gap position of $v_{\min}$ is roughly constant for the lower two shear rates but continues to propagate toward the inner wall for a short duration for $\dot{\gamma} = 0.5\,s^{-1}$.

As the period of flow reversal ends, two distinct bands appear; the interface position between these two regions is shown with outlined symbols in Fig. 7. Note the interface remains in approximately the same position even after long acquisition times (Fig. S14 [59]), and that this interface position stabilizes far before the stress reaches a stable value (Figs. 4, S16b,d). The relative stability of the interface position will be analyzed further as the behavior of this fluid is categorized in the *Discussion*. The relative size of each band often follows a lever rule in yield stress fluids [16] and WLMs exhibiting shear banding [92]. In the lever rule, the band interface position increases linearly with the applied shear rate. Although here the band interface increases monotonically with the shear rate, a linear relationship is not observed; the interface position predicted using the lever rule while accounting for wall slip matches the measured values at low shear rates but deviates at high shear rates (Fig. S15 [59]). Deviations from the lever rule are not uncommon in shear banding systems [26,37,93–95], particularly when wall slip is significant [61,91] like in this system. Furthermore, here the band interface position is sensitive to the magnitude of the maximum stress in the overshoot region (Figs. S6 and S14 [59]) and gap size of the geometry (Fig. S16 [59]), suggesting that this heterogeneous flow may form in a manner more consistent with band formation in yield stress fluids instead of traditional WLMs (see *Discussion*).

The significant elastic recoil during startup generates strong heterogeneities in the local shear rate of the fluid, illustrated by the evolution of the local shear rate near the inner wall and outer wall, $\dot{\gamma}_H$ and $\dot{\gamma}_L$, respectively (Fig. 8). These quantities were estimated by performing linear fits of the velocity profile near each wall; see details in SI.17 and Fig. S17 [59]. With increasing strain, the shear rate near the inner wall increases as the velocity profile becomes nonlinear; the local shear rate quickly rises as flow reversal becomes significant, achieving a maximum just after maximum flow reversal time t^* [$\star$ in Fig. 8(a)]. This transition is most dramatic for $\dot{\gamma} = 0.02\,\mathrm{s}^{-1}$, where $\dot{\gamma}_H$ grows to nearly 50-fold the applied shear rate, $\dot{\gamma}_{app}$. At the higher shear rates, $\dot{\gamma} = 0.1\,\mathrm{s}^{-1}$ and $\dot{\gamma} = 0.5\,\mathrm{s}^{-1}$, $\dot{\gamma}_H$ increases more modestly ($\dot{\gamma}_H \sim 8\dot{\gamma}_{app}$). As the velocities become less negative and distinct flow regions form, $\dot{\gamma}_H$ decreases to between four- and sixfold of the applied shear rate in each case, similar to shear banding WLM systems [22,90].

The shear rate near the inner wall varies not only with time but also with applied shear rate. The absolute magnitude $\dot{\gamma}_H$ at long times (or large γ) increases with the applied shear rate: $\dot{\gamma}_H \approx 0.1$, 0.4, and 2 for $\dot{\gamma} = 0.02$, 0.1, and $0.5\,\mathrm{s}^{-1}$, respectively. Increasing $\dot{\gamma}_H$ with the applied shear rate (or *Wi*) is common in shear banding WLMs where significant wall slip is present [40,91,94]. Additionally, the shear rate in the fluidized region is not constant and instead decreases with increasing gap position because of the inherent stress gradient in the concentric cylinder geometry and shear thinning behavior of the WLMs [96]. The extent to which the shear rate varies in the fluidized region strongly depends on the width of this region. Accordingly, little variation in local shear rate is observed in the fluidized region at low applied shear rates, whereas an almost two-order of magnitude decrease in shear rate is observed across this region at $\dot{\gamma} = 1$ and $2\,\mathrm{s}^{-1}$ (Fig. S18 [59]).

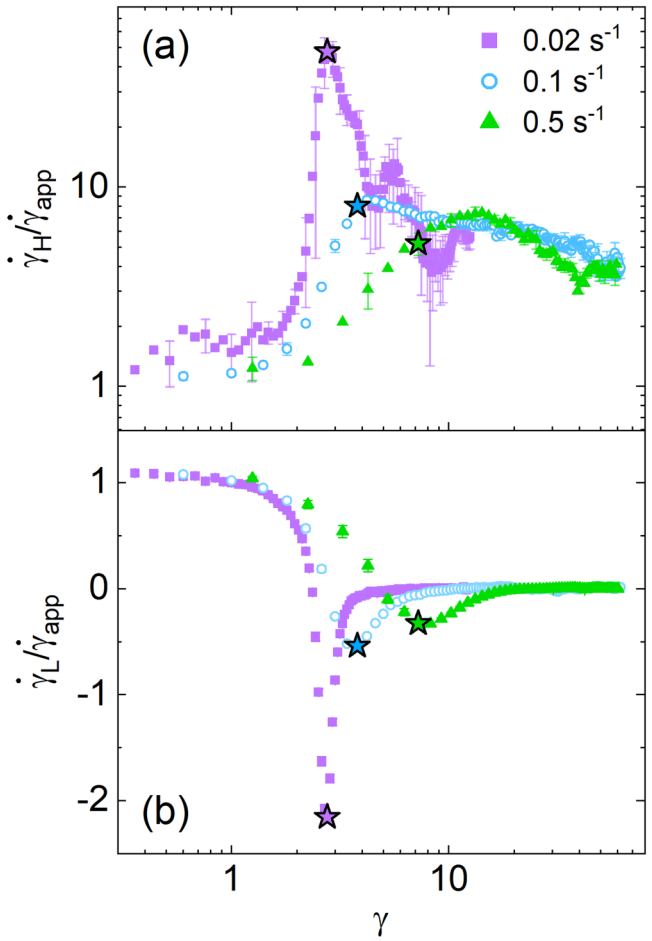

FIG. 8. Evolution of the local shear rate normalized by the applied shear rate $\dot{\gamma}_{app}$ near the (a) inner wall, $\dot{\gamma}_H$, and (b) outer wall, $\dot{\gamma}_L$ with increasing strain; ★ denotes values at t^*. Error bars are shown every third point for visual clarity.

The shear rate near the outer wall, $\dot{\gamma}_L$, decreases with increasing strain, quickly becoming negative as flow begins reversing [Fig. 8(b)]. The magnitude of $\dot{\gamma}_L$ is greatest at the same strain (and time) of maximum elastic recoil ($v_{min} = v^*$). Similar to the trends observed for the normalized inner wall local shear rate, the normalized outer wall local shear rate, $\dot{\gamma}_L/\dot{\gamma}_{app}$, varies the most for $\dot{\gamma} = 0.02\,\mathrm{s}^{-1}$ and varies less with increasing shear rate. At high strains when velocities become less negative, $\dot{\gamma}_L$ approaches zero regardless of the applied shear rate, indicating that a large portion of the fluid near the outer wall is practically immobile. Small yet measurable multidimensional perturbations of the fluid in this region are observed after band formation, which are attributed to the development of secondary flows at longer times (see Sec. III C 4).

4. Elastic instabilities

The high elasticity of these WLMs promotes the formation of elastic instabilities following formation of fluidized and immobile regions. These elastic instabilities generate 2D or 3D secondary flows and fluctuations of the band interface and have been reported extensively in WLM systems [24,40,42,43,61,97]. In these works, flow visualization along the vorticity axis was utilized to characterize these elastic instabilities. Although such visualization is not performed here, evidence of elastic instabilities appears in the flow-flow gradient plane data captured by PTV for $\dot{\gamma} = 0.02$, 0.1, and $0.5\,\mathrm{s}^{-1}$. Two-dimensional flow, with particle motion perpendicular to the flow direction, is apparent as the flow evolves; see SI.22.2 [59] for video. Note that little can be said about fluctuations along the vorticity axis (see *Discussion*), although no change in particle focus due to vorticity-direction motion is observed for $\dot{\gamma} = 0.02$, 0.1, and $0.5\,\mathrm{s}^{-1}$, unlike at higher shear rates where 3D flows do occur ($\dot{\gamma} = 2\,\mathrm{s}^{-1}$, SI.22.4 [59]).

While elastic instabilities in WLMs are typically characterized based on direct flow visualization along the vorticity axis, here elastic instabilities are analyzed via particle displacements in the nonfluidized region. This approach was selected due to a few practical limitations (see SI.19.1 [59]), and while atypical, fluctuations in the low shear rate band have been examined previously via SANS in shear banding fluids [27,28,35]. Tracking particle displacement in the nearly immobile region is possible here because of the limited motion of this region. Particles within this region remain in the PTV observation window throughout the experiment duration; therefore, single particles can be tracked continuously during startup, illustrated in Fig. 9 for $\dot{\gamma} = 0.5\,\mathrm{s}^{-1}$.

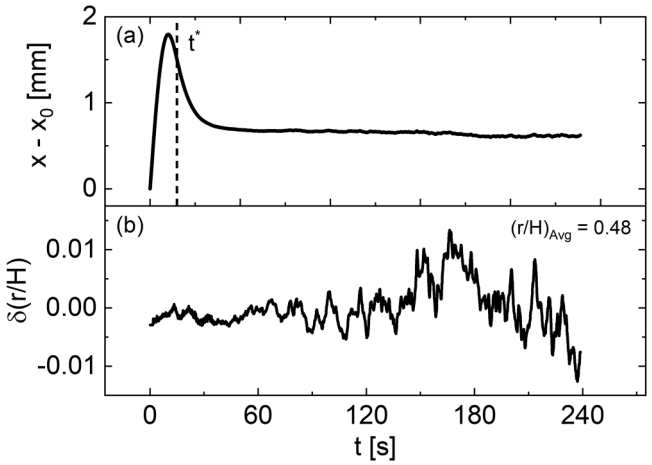

FIG. 9. A single tracer particle's (a) displacement from its initial position and (b) deviations in normalized gap position from its average $(r/H)_{avg} = 0.48$ with time at $\dot{\gamma} = 0.5\ s^{-1}$. Radial fluctuations grow significantly after flow reversal. Dashed line in (a) indicates the time when flow reversal is greatest, t^*.

The total displacement $x(t) - x_0(t = 0)$ of the particle near the onset of startup flow [Fig. 9(a)] captures the initial elastic deformation, flow reversal, and terminal low shear rate motion. These long-duration trajectories allow direct observation of spatial fluctuations that arise from additional elastic instabilities during startup [Fig. 9(b)]. Here, radial fluctuations are quantified as deviations $\delta(r/H)$ from the particle's average gap position $(r/H)_{avg}$.

At early times ($t < 50$ s), before and during flow reversal, radial fluctuations of the particle position are small. As the fluidized and nonfluidized regions become distinct ($t > 50$ s), these fluctuations grow in magnitude. The motion of particles can be compared in both time and space throughout the $r - \theta$ plane because the particles do not move appreciably throughout the experiment. Comparing the temporal fluctuations of particles in the nearly immobile region during shear startup reveals strongly correlated radial fluctuations along the flow gradient direction (radial axis, Fig. 10) but significant variation in the flow direction (azimuthal axis, Fig. 11). Note the radial fluctuations shown in Figs. 10(c)–10(d) and 11(c)–11(d) are normalized by their root-mean-square value $\tilde{\delta}(r/H) = \delta(r/H)/\delta(r/H)_{RMS}$ and shifted by a constant a_{shift} for facile comparison.

The radial fluctuations of particles with approximately constant azimuthal position at shear rates $\dot{\gamma} = 0.02\ s^{-1}$ [Figs. 10(a) and 10(c)] and $0.5\ s^{-1}$ [Figs. 10(b) and 10(d)] evolve almost identically in time, with peaks and valleys occurring in unison; however, fluctuations are much less regular at the higher shear rate. Note similar coordinated motion is observed at $\dot{\gamma} = 0.1\ s^{-1}$ (Fig. S19 [59]). Here, the azimuthal position of particles is defined by θ^*, where θ^* is a normalized angle such that $0 < \theta^* < 1$ in the observation window: $\theta^* = 0$ at the right boundary of the image and $\theta^* = 1$ at the left. Given the irregularities in the fluctuations at higher rates, two groups of particles are shown for $\dot{\gamma} = 0.5\ s^{-1}$. Despite that the two particle groups are well-separated from one another ($\theta^* = 0.24 - 0.27$ and

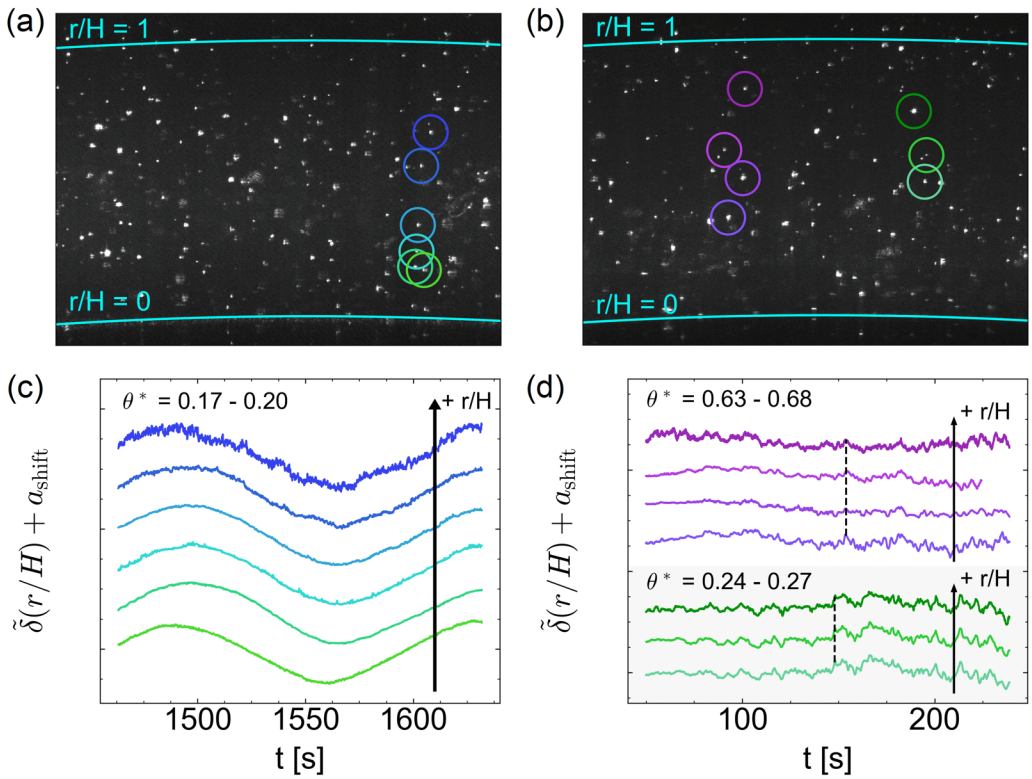

FIG. 10. Image showing sets of particles over a brief window of time during startup at (a) $\dot{\gamma} = 0.02\ s^{-1}$ and (b) $\dot{\gamma} = 0.5\ s^{-1}$ that vary in gap position r/H at approximate constant azimuthal position θ^*, where θ^* is the azimuthal angle normalized such that $0 < \theta^* < 1$ in the observation window: $\theta^* = 0$ at the right boundary and $\theta^* = 1$ at the left. The corresponding normalized radial deviations from the mean $\tilde{\delta}(r/H) = \delta(r/H)/\delta(r/H)_{RMS}$ are shown below each image in (c) and (d). Fluctuations are highly coherent with constant θ^* at both shear rates [dashed guidelines are provided to help illustrate this point in (d)].

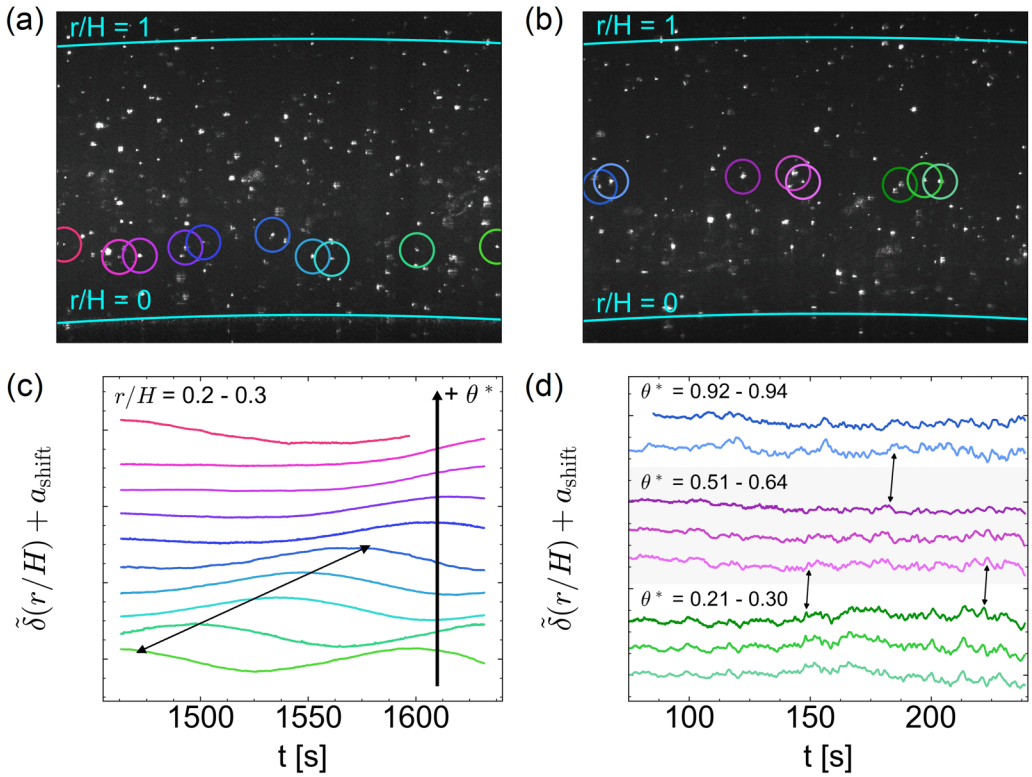

FIG. 11. Image showing sets of particles during startup at (a) $\dot{\gamma} = 0.02\,\mathrm{s}^{-1}$ and (b) $\dot{\gamma} = 0.5\,\mathrm{s}^{-1}$ that vary in azimuthal position θ^*, where θ^* is the azimuthal angle normalized such that $0 < \theta^* < 1$ in the observation window: $\theta^* = 0$ at the right boundary and $\theta^* = 1$ at the left. The corresponding normalized radial deviations from the mean $\tilde{\delta}(r/H) = \delta(r/H)/\delta(r/H)_{RMS}$ are shown below each image in (c) and (d). Fluctuations are lag in time in both shear rates and are less coherent at $\dot{\gamma} = 0.5\,\mathrm{s}^{-1}$ in the flow direction (d) compared to the radial direction [Fig. 10(d)]. The double-head arrows in (c) and (d) demonstrate the propagation of radial disturbances in the flow direction.

$\theta^* = 0.63 - 0.68$), the uniform behavior between particle groups at constant θ^* suggests that this coherent behavior occurs regardless of the azimuthal angle. Note that while most prominent features align, some discrepancies across particles arise due to experimental noise such as brightness variations that impact the computed centroid of the particle.

In contrast, particles of approximately equal radial coordinate $(r/H) \approx 0.25$ at $\dot{\gamma} = 0.02\,\mathrm{s}^{-1}$ and $(r/H) \approx 0.5$ at $\dot{\gamma} = 0.5\,\mathrm{s}^{-1}$ do not fluctuate with the same degree of similarity as those with constant θ^* [Figs. 11(a) and 11(b)]. At $\dot{\gamma} = 0.02\,\mathrm{s}^{-1}$, the shape of the fluctuations are largely similar across the width of the observation window but are offset by a time lag [Fig. 11(c)]. However, at $\dot{\gamma} = 0.5\,\mathrm{s}^{-1}$, the shape of the fluctuations become increasingly dissimilar as the difference in the azimuthal coordinate grows [Fig. 11(d)]. Within a particular azimuthal cluster of particles [Fig. 11(b)], fluctuations are largely coherent; however, only a few similar peaks and valleys are identifiable between clusters, emphasized by double-headed arrows in Fig. 11(d). Like at the lower shear rate, a time offset is present between these common features. At both shear rates, the radial fluctuations of particles downstream (greater θ^*) lag behind, suggesting that the radial fluctuations result from a disturbance that propagates in the flow direction.

Estimates of the lag time between fluctuations using simple visual translation and overlay of features—like those indicated by double arrows in Figs. 11(c) and 11(d)—and the cross-correlation spectral density (SI.19 [59]) reveal that the disturbance travels at a speed close to the near-wall velocity of the fluidized region. Therefore, these radial fluctuations in the low shear rate band are likely generated by the fluidized region and propagate outward into the nonfluidized region. The highly elastic character of the low shear rate band propagates these disturbances, resulting in the high degree of coherence along the radial axis, whereas in the flow direction new disturbances are generated and attenuated by the fast-moving fluid in the fluidized region. This description agrees with the video of the flow behavior (SI.22.2 [59]). Note that the agreement of the disturbance speed with the near-wall fluid velocity also rules out geometry defects or misalignment inducing these fluctuations; the propagation speed is less than the wall speed and significantly less when wall slip is present.

Interestingly, the magnitude of radial fluctuations within the nonfluidized region grows and subsequently decays as the stress evolves. The radial fluctuations in the low shear rate band during startup following the stress overshoot are illustrated in Fig. 12 for $\dot{\gamma} = 0.02$, 0.1, and $0.5\,\mathrm{s}^{-1}$. Here, the dependence of radial fluctuations on gap position is quantified using a collection of particles in the low shear rate band; the root-mean-square radial deviations of particle trajectories $\delta(r/H)_{RMS}$ are averaged over bins covering one-tenth the gap width. The magnitude of fluctuations is greatest near the interface between fluid regions and decay toward the stationary outer wall [increasing r/H, Figs. 12(d)–12(f)]. While the overall magnitude of the radial position (and stress)

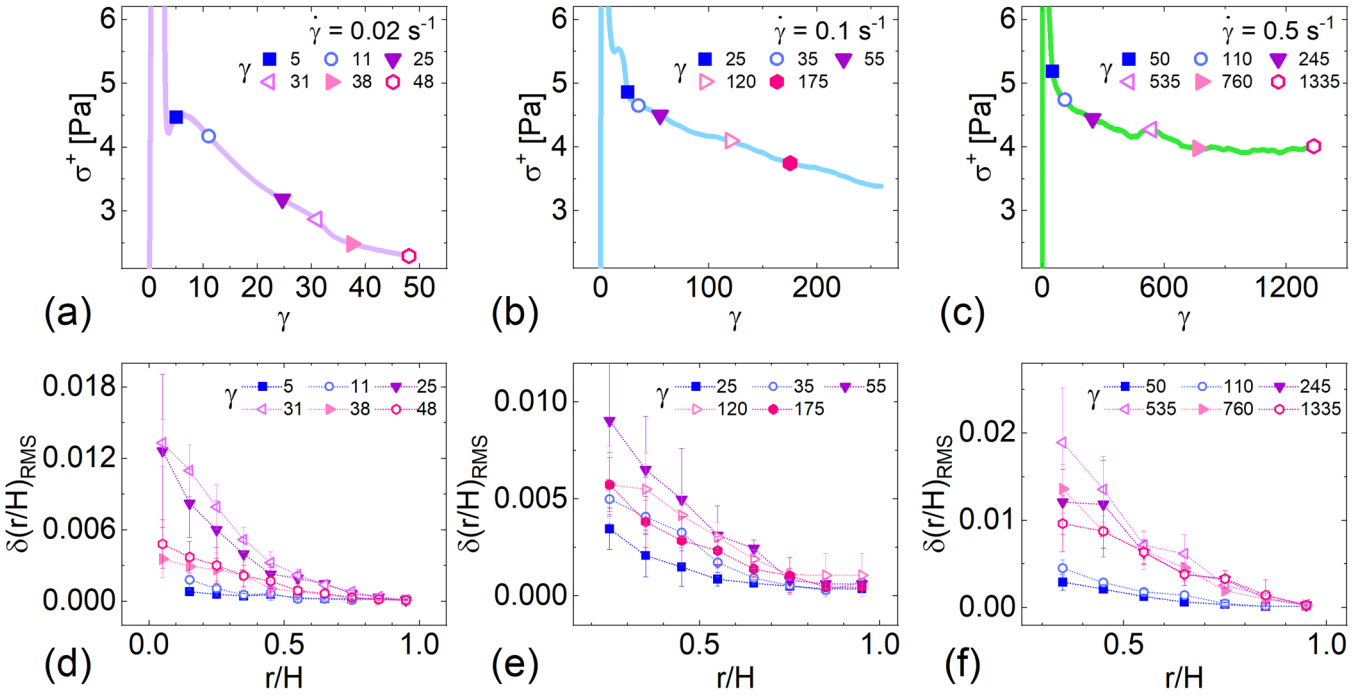

FIG. 12. (a)–(c) Evolution of the stress at $\dot{\gamma} = 0.02$, 0.1, and $0.5\,s^{-1}$ and (d)–(e) corresponding root-mean-square deviations in radial gap position $\delta(r/H)_{RMS}$ with increasing strain. Fluctuations are greatest near the interface between the fluidized and nonfluidized regions and decrease in magnitude toward the outer stationary wall $(r/H) = 1$.

fluctuations is greatest at $\dot{\gamma} = 0.5\,s^{-1}$, radial fluctuations are comparable in magnitude at $\dot{\gamma} = 0.02$ and $0.1\,s^{-1}$. Interestingly, the magnitude of the fluctuations is smallest immediately following the stress overshoot (blue ■, Fig. 12), in line with previous studies on CTAB/NaSal WLMs that noted flow reversal occurs before the onset of significant secondary elastic instabilities [48,49].

Remarkably, the evolution of fluctuations in time (or strain) is nonmonotonic for all three shear rates, with radial fluctuations achieving a maximum value before decreasing at long times [Figs. 12(d)–12(f)]. To better illustrate this trend, the magnitude of radial fluctuations in the nonfluidized region closest to the interface between fluid regions in Figs. 12(d)–12(f) are examined versus strain (Fig. 13). The rise and subsequent fall in the fluctuation magnitude occur while the stress is, on average, decreasing [Figs. 12(a)–12(c)], though some fluctuations in the stress response are observed in this region. Qualitatively, the scattering of light from particles in the fluidized band becomes increasingly anisotropic as the fluctuations evolve (Fig. S23 [59]), suggesting the evolution of these fluctuations could be related to the WLM alignment.

The radial fluctuations of particles in the nonfluidized band of fluid are much less regular at $\dot{\gamma} = 0.5\,s^{-1}$ compared to $\dot{\gamma} = 0.02\,s^{-1}$. The regularity of radial fluctuations at $\dot{\gamma} = 0.1\,s^{-1}$ is intermediate to these two shear rates (Fig. S19 [59]). The increasing irregularity of these radial fluctuations in the nonfluidized band does not correlate to any significant stress fluctuations. However, as shear rate is increased further to $\dot{\gamma} = 1$ and $2\,s^{-1}$, the stress response fluctuates significantly after about $t \approx 500$ s (Fig. S7 [59]). These stress fluctuations are accompanied by highly spatially- and temporally complex 3D flows, which together are signatures of elastic turbulence [43]; see SI.22.4 [59], for example, video. Additionally, at the end of these experiments, significant sample air entrainment and rod climb were also observed (Fig. S3 [59]), suggesting the air-sample interface has also potentially fractured (Fig. S10 [59]).

IV. DISCUSSION

A. Fluid characteristics of both WLMs and yield stress fluids

The wealth of complex flow behaviors including flow reversal, wall slip, and elastic instabilities exhibited by this

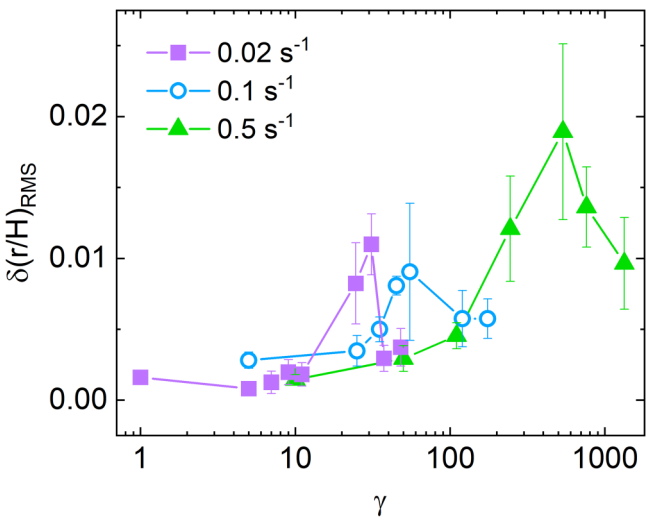

FIG. 13. Evolution of root-mean-square deviations in radial gap position $\delta(r/H)_{RMS}$ closest to $r/H = 0$ with increasing strain at $\dot{\gamma} = 0.02$, 0.1, and $0.5\,s^{-1}$. The magnitude of radial fluctuations begins to grow at strains corresponding to the end of the stress overshoot and decreases at large strains (long times).

system result from the combination of the high elasticity of the WLMs and their apparent yield stress. Some characteristics of this system and its flow behavior resemble that expected from traditional WLMs. First, the shear rate measured in each controlled-stress experiment below the static apparent yield stress approaches a constant value after approximately 20 min (Fig. S5 [59]); in a true yield stress fluid with viscoelastic aging or thixotropy, viscosity bifurcation is typically observed, where the shear rate eventually collapses to zero [86,98]. Notably, each of the applied stresses, which span a decade in magnitude, produces a distinct shear rate value. Because the viscosities plateau in time —rather than continually increase [99]—to the same value for each applied stress, these measurements may be accessing a true zero-shear viscosity. This "apparent" yield stress has been noted in other WLM gels with exceedingly slow dynamics [1,2,53], although under practical flow conditions this distinction is unimportant. Interestingly, despite exhibiting a yield stress, LAOS measurements of these poloxamer WLMs (Fig. S24 [59]) display strain thinning behavior expected in entangled polymer melts and solutions; no local maximum in G'' is observed, a distinct feature in LAOS of soft glassy materials which have yield stresses [100]. An additional characteristic typical of WLMs is the elastic instabilities that manifest after flow reversal, which become increasingly irregular and even turbulent with increasing shear rate (discussed further in Sec. IV E).

However, certain characteristics of the flow more closely resemble those observed in yield stress fluids, including the presence of a practically immobile, solid-like band of fluid. In most reports of WLMs exhibiting shear banding, the low shear rate band still flows, exhibiting a small but nonzero velocity [11,22,26,35]. Additionally, this immobile region of fluid persists even at high shear rates on the flow curve, accompanied by a large degree of shear thinning in the fluidized region (Fig. S7 [59])—similar to behavior reported in some yield stress fluids [17,86,101]. Conversely in traditional WLMs, shear bands with a discontinuous band interface give way to homogeneous, shear thinning flow at high shear rates [26]. Furthermore, as will be discussed next, the mechanism of heterogeneous flow formation bares strong resemblance to that observed in yield stress fluids exhibiting stable shear bands.

B. Fluid classification and proposed mechanism of flow heterogeneity

Divoux *et al.* [16] proposed three categories of fluids exhibiting shear banding or shear localization; this framework is employed to propose a classification for this fluid. In the first category, which describes the "classical" WLM shear banding, fluids undergo a mechanical instability or shear-induced phase transition in which the flow separates into bands of distinct, nonzero shear rate. The flow curve exhibits a Newtonian region at low shear rates followed by an unstable, shear banding plateau region bound by two critical shear rates. Here, P234 WLMs have a static yield stress and an immobile low rate band—and homogeneous flow is not recovered at shear rates beyond the apparent plateau region ($\dot{\gamma} < 0.02\,\mathrm{s}^{-1}$) on the flow curve—inconsistent with the behavior in this first category of fluids. Additionally, in these P234 WLMs, the interface between fluidized and nonfluidized flow regions is highly sensitive to the stress gradient of the geometry, determined by the curvature and gap width. WLMs that shear band due to a constitutive instability can also be sensitive to the gradient in shear stress, but much larger geometry differences are required to see significant changes [102]. In this system, the interface position, $(r/H)_{int}$, in startup flow at $\dot{\gamma} = 0.1\,\mathrm{s}^{-1}$ is twice as large with a gap size of 0.5 mm versus with a gap of 1.15 mm (Fig. S18 [59]).

Most notably, the shear banding mechanism in canonical WLMs appears to be different than that observed in these P234 WLMs. In canonical WLM solutions, shear bands are hypothesized to form following a "disentangle, re-entangle" mechanism as suggested by PTV and flow-small angle neutron scattering [22,27]. In brief, the large stress built up during the initial elastic deformation leads to bulk disentanglement of the WLMs throughout the geometry and a drop in the stress (decreasing portion of the stress overshoot). As time progresses, fluid closer to the stationary outer cylinder re-entangles, whereas fluid closer to the moving inner cylinder remains disentangled, and shear bands form. While the WLMs in this work likely disentangle in the stress overshoot region, in the "disentangle, re-entangle" mechanism [22,27], the heterogeneous shear bands always form *after* the stress overshoot has subsided. Conversely, the flow heterogeneity and initial band formation in this work occur during the decay in stress in the primary overshoot region.

Divoux *et al.* [16] also outlines two types of yield stress fluids (YSFs) that can exhibit flow heterogeneity: YSFs exhibiting stable shear banding (deemed category 2) [20,21] and those like Carbopol [19,32] following Herschel–Bulkley rheology (monotonic constitutive relationship) that exhibit long transient shear bands but eventually recover the homogeneous flow (category 3). Both type 2 and 3 fluids exhibit velocity profiles during the heterogeneous flow that are similar in shape to each other and to the P234 WLMs herein, with one fluidized band and one immobile band. Additionally, in category 2 and 3 yield stress fluids, heterogeneous regions of fluid form *during* the rapid decrease in stress after initial elastic deformation [19–21], just as occurs in P234 WLMs. While the flow behavior in these P234 WLM gels resembles that of YSFs, distinguishing between category 2 and 3 fluids can be difficult, as both types of fluids can exhibit similar heterogeneous flow behavior over long time scales. Notably, category 2 fluids are said to exhibit "shear banding," whereas often fluids in category 3 are described via "shear localization" or as "transient shear banding" only [17,19,103].

We propose that the mechanism of shear band formation in the startup flow in these poloxamer WLMs is most similar to that of aging soft glassy materials in category 2, as key features of these P234 WLM gels are inconsistent with experimental results on Carbopol microgels exhibiting category 3 behavior [19,32]. Unfortunately, the behavior of fluids in category 2 is not well-understood, and the shear banding in these YSFs is thought to result from wide-ranging phenomena: a mechanical instability that drives nonmonotonic flow

curves (constitutive instability), shear-induced phase transitions, competition between shear and attractive interactions between constituents, flow-concentration coupling, and/or thixotropic behavior [16,32,66,104–107]. Notably, a number of category 2 fluids exhibit viscoelastic aging (like in our system). Authors of studies examining these fluids often propose that these fluids exhibit stable shear banding due to two different mechanisms: mechanical instability (shear rates within the unstable region) and transient shear banding trapped by aging (shear rates above the unstable region) [20,21]. Though the authors propose that these behaviors are distinct mechanisms of banding [20,21], there is no experimental signature to indicate one mechanism over the other.

As the behaviors of category 2 fluids are not universally well-understood, we instead aim to rule out category 3 behavior by comparing our results with experimental features detailed by Divoux on category 3 fluids [19,32,108]. As mentioned in the *Results*, numerous metrics suggest that the P234 WLMs here do not fluidize at long times and instead exhibit stable shear bands, as key features in the startup stress response are indicative of fluidization in category 3 fluids. For example, in category 3 Carbopol microgels exhibiting transient banding during controlled shear rate tests, the velocity profiles and band interface positions both evolve continuously with decreasing stress until fluidization occurs [19,32]; conversely in P234 WLMs, the band interface position becomes permanent well before stress stops decaying (Fig. 4, S14). Notably, the band interface position in these transiently banding microgels continuously evolves to larger gap positions and is accompanied by decreasing amounts of wall slip, until full fluidization occurs [19,32,108]. However in P234 WLMs, the opposite occurs: the interface between bands stabilizes at gap positions smaller than that for maximum flow reversal (Fig. 7) and wall slip becomes far more, not less, significant in time (Fig. 6).

Finally, the key feature of the fluidization event in Carbopol gels is a dramatic drop in the stress (distinct from the stress overshoot) following a nearly stable region in the stress response. This fluidization event occurs concomitantly with a significant increase in the degree of wall slip. In P234 WLMs, a similar decrease in stress at long times is often observed [Figs. 4(a), S16c]; however, this rapid stress decay corresponds only to slip (see $\dot{\gamma} = 0.02\ \mathrm{s}^{-1}$, Fig. 6), and a fluidization event is never observed. In fact, the band interface position barely changes after maximum flow reversal time t^* for shear rates spanning two decades in magnitude (Fig. S13 [59]). However, slip becomes significant at a range of times following t^* (Fig. 6), suggesting that here, the presence of slip is uncorrelated to flow reversal and to when the interface stabilizes or destabilizes. Unfortunately, longer-time startup measurements would be required to definitively differentiate between these two behavior types; however, these measurements cannot be performed accurately due to evaporation effects.

C. Stable shear banding: Nonmonotonic flow curve versus transient bands permanently trapped due to aging

As aforementioned, the steady shear bands in the category 2 fluids can result from a wide range of phenomena including viscoelastic aging. Martin and Hu [20] examined a Laponite suspension with a yield stress, where a constitutive instability is predicted based on the flow curve. The authors observe the heterogeneous flow in the nonmonotonic region of the flow curve, deemed "shear banding." The authors also observe stable heterogeneous flow at shear rates beyond the nonmonotonic region, deemed transient shear banding permanently "trapped" due to aging, that cannot be distinguished experimentally from bands formed due to constitutive instability. Similarly, Kurokawa *et al.* [21] refer to heterogeneous flow occurring at shear rates beyond where the constitutive instability occurs as "steady-state shear banding trapped by aging," with the caveat that this type of shear banding should be distinguished from shear banding resulting from the intrinsic flow instability.

Martin and Hu [20] identified two key components for trapped transient banding to occur, which are satisfied in P234 WLMs examined here. First, shear bands must form transiently. Like in simple yield stress fluids [109], the heterogeneous flow initially develops because of the inherent stress gradient of the concentric cylinder geometry; the stress exceeds the static yield stress during the stress overshoot, leading to fluidization. However, due to the stress gradient, this fluidization is localized closer to the inner cylinder and ceases as the stress drops below the static yield stress—before the entirety of the gap is able to fluidize. Evidence of this mechanism of heterogeneous flow formation is observed in this system; in addition to the aforementioned dependence of the band interface position on the gap width, the interface is sensitive to the magnitude of the stress overshoot. Across replicate startup trials at $\dot{\gamma} = 0.02$ and $0.01\ \mathrm{s}^{-1}$, slightly larger fluidized regions (Fig. S14 [59]) were correlated with larger magnitudes of the stress overshoot (Fig. S6 [59]).

The second criterion proposed by Martin and Hu [20] is that the yield stress must increase with aging time. Supplemental aging studies at 39 °C suggest an aging time-temperature similarity (SI.1, SI.10 [59]), illustrating that P234 WLMs aged for shorter times at 39 °C can replicate the properties of P234 aged for longer times at 38.5 °C. Additional flow curve measurements at 39 °C (accelerated rate of aging) suggest that the dynamic yield stress does increase with aging and t_w (Fig. S2 [59]). Thus, after the heterogeneous flow forms, the nonfluidized region in these P234 WLMs continues to age, becoming more resistant to flow and trapping the shear banded flow.

Although at moderate shear rates the shear bands persist permanently, trapped transient banding at high shear rates eventually gave way to the homogeneous flow in these prior studies [20,21]. The lifetime of the transient bands also decreased with increasing shear rate. In these poloxamer WLMs, a similar effect could be possible but could not be tested experimentally due to the onset of elastic turbulence at high shear rates. Supplemental 1-2 plane flow-SANS measurements provide additional evidence of this proposed mechanism, where a trapped banded structure is observed at lower shear rates, whereas transient banding (Fig. S26 [59]) and full fluidization are observed at higher shear rates (Fig. S27 [59]); however, given that the SANS geometry differs and that reproducing the exact aging conditions in

these measurements is difficult, we refrain from making direct comparisons.

A number of category 2 fluids are proposed to exhibit both banding in an unstable region of the flow curve and transient shear banding trapped by aging; both behaviors are feasible here. The critical shear rate separating band formation due to these two behaviors was determined previously in aging Laponite suspensions as the lowest observed average shear rate in the high shear band [20]. Estimating this value from PTV at lowest shear rate, $\dot{\gamma} = 0.02\,\mathrm{s}^{-1}$, yields $\dot{\gamma}_c = 0.1 \pm 0.02\,\mathrm{s}^{-1}$. As such, the constitutive curve may be nonmonotonic below this shear rate. Notably, at the two shear rates below $\dot{\gamma}_c$ ($\dot{\gamma} = 0.02,\ 0.1\,\mathrm{s}^{-1}$), the interface between bands is sharp and minimal shear thinning occurs in the high shear rate band (Fig. S18 [59]). Additionally, the band interface position at these two shear rates agrees with the value predicted by the lever rule after accounting for wall slip (Fig. S15 [59]), whereas deviations occur at higher rates —suggesting that a nonmonotonic flow curve is at least feasible for these lower rates. Conversely, at shear rates above $\dot{\gamma}_c$, an immobile fluid region persists and substantial shear thinning occurs across the fluidized region (Fig. S18 [59]). Unlike in traditional shear banding fluids, no sharp interface is observed between regions when $\dot{\gamma} \geq 1\,\mathrm{s}^{-1}$. Therefore, constitutive-instability-driven shear banding does not seem likely at shear rates above $\dot{\gamma}_c$.

D. Criteria for flow reversal

While the shear band formation in poloxamer WLMs resembles that observed in aging materials like Laponite suspensions and Ludox gels, flow reversal was not reported in either of these systems. In fact, flow reversal is rarely observed in yield stress fluids and WLMs; limited reports in yield stress fluids include Carbopol microgels [30] and physically associating triblock polymer gels [47]. In both of these cases, the fluid velocity during flow reversal reached substantial magnitudes: nearly half the imposed boundary velocity in Carbopol and equal to the imposed velocity in the polymer gel. In these systems, the flow reversal was attributed to sample fracture either in the bulk or at an interface; note that flow reversal observed in poloxamer WLMs here has distinct rheological features from fracture phenomena, which only occurs in these systems if a different pretreatment is applied to further age the system (SI.10 [59]). Flow reversal has been observed previously only in CTAB/NaSal WLMs [44,48,49]. In these studies, the magnitude of flow reversal was much smaller, reaching at maximum roughly half of the imposed wall velocity versus over twofold the imposed wall velocity observed here. In most cases, flow reversal in the CTAB/NaSal WLMs eventually led to the shear banded flow, but evidence of sample fracture was observed occasionally [48].

Why is flow reversal observed in so few systems? In many systems, flow reversal might be short-lived or of small magnitude and, therefore, difficult to observe, or be absent entirely. In all of the soft matter systems we were able to identify that exhibit flow reversal [30,44,45,47–49,110], this phenomenon occurs while the stress is rapidly decreasing following the stress overshoot in startup flow. For flow reversal to occur while stress is being relaxed within the system, we propose that two criteria should be satisfied. First, the system must have elasticity; flow reversal is a retraction of fluid after the initial elastic deformation in the startup flow and, therefore, some portion of the initial deformation must be recoverable. This criterion is consistent with prior reports that high *El* is required to observe flow reversal in WLMs [48,49], and that flow reversal occurs in Carbopol microgels following a period of elastic loading and subsequent sample failure [30].

Second, the heterogeneous flow is likely necessary while the stress decreases in the stress overshoot region, where each region of fluid relaxes stress at a different rate. Flow reversal occurs in these systems because the region of fluid near the inner wall yields and dissipates stress. However, the outer region of fluid relaxes stress more slowly and, therefore, recovers some elastic strain to match the rate of stress dissipation of the fluidized region. This idea can be understood more clearly by considering an elastic yield stress fluid; upon partial fluidization, the unfluidized region will retract like an elastic solid as the stress decreases. A similar argument applies in the case of fracture, except the stress is quickly dissipated in a much smaller region—either in a small region of the bulk as seen in associating polymer gels [47] or at an interface as seen in Carbopol gels [30].

Note while these criteria are likely necessary for flow reversal based on experimental evidence and the above rationale, they may not be sufficient. For example, if the outer band of fluid had a finite shear rate instead of being immobile like in these poloxamer WLMs, then flow reversal could be masked by the underlying flow, particularly at high shear rates where flow reversal is small. Additionally although general, these criteria are consistent with observations in systems like WLMs where properties like entanglement density and ramp up rate are reported to impact flow reversal [48,49], as these two properties are expected to influence the elasticity of the fluid and the severity of the flow heterogeneity as the stress decreases in the overshoot region, respectively.

These criteria can be used to rationalize why flow reversal is seldom observed. In thixotropic fluids with minimum elasticity, partial fluidization during the stress overshoot may occur, but if the elasticity is small, flow reversal may not be present or may be too small to measure. In WLMs, the "disentangle, re-entangle" mechanism [22,27] and corresponding microstructural evidence suggest homogeneous disentanglement in the stress overshoot region. This homogeneity in the flow fails to satisfy the second criteria of heterogeneity immediately following the maximum stress in the stress overshoot region. As aforementioned, disagreement with the "disentangle, re-entangle" mechanism does not imply that the P234 WLMs gels do not disentangle upon flow startup. Instead, the emergence of shear bands (flow heterogeneity) in this mechanism occurs on much longer time scales, after the stress overshoot. In contrast, fluidization and flow heterogeneity in these WLM gels are introduced *during* the stress overshoot, which may result from microstructural changes like disentanglement, localized primarily in the fluidized region.

Therefore, poloxamer WLMs examined here likely exhibit pronounced flow reversal because of their high elasticity and because the flow heterogeneity is induced during the stress overshoot like in yield stress fluids. Interestingly, the flow kinematics in these poloxamer WLMs evolve similarly to VCM and GCB models because of when the flow heterogeneity is introduced: in these models, the flow similarly becomes heterogeneous in the stress overshoot region immediately following the maximum stress. Startup flows simulated by these models both predict a rapid increase in the breakage rate at the stress overshoot, creating two regions with starkly different distributions of micelle lengths [50,51], and subsequently different effective stress relaxation rates. The duration of flow reversal in these models is a function of the WLM breakage rate and relaxation time of the shorter-length WLMs. Here, the duration of flow reversal is then likely related to the relaxation time of the fluidized region. Presumably, CTAB/NaSal WLMs also deviate from the homogeneous "disentangle, re-entangle" mechanism proposed for many WLMs—an interesting hypothesis meriting future investigation.

E. Elastic instabilities

The elastic instabilities observed in these poloxamer WLMs concomitant with shear banding are often observed in WLMs, and numerous studies have been dedicated to characterizing their origin and evolution [24,39–41]. For completeness, we briefly note that these secondary flows are not the result of inertially driven Taylor instabilities observed in Newtonian fluids at high Reynolds numbers [111]. For example, using an approximate viscosity of the fluidized region calculated from the stress and the local shear $\dot{\gamma}_H$ rate at $\dot{\gamma} = 0.5\,\mathrm{s}^{-1}$, Reynolds number is estimated to be $Re \sim O(10^{-4})$ in the fluidized region. Therefore, inertial effects are negligible.

Secondary flows in WLM solutions are often attributed to a bulk elastic instability arising in curved flow geometries that leads to the formation of Taylor-like vortices [112]. In shear-banded flows, this elastic instability is typically localized in the high-shear-rate band of fluid and destabilizes the interface between shear bands, yielding undulations of the band interface along the vorticity axis [39,48,97,113]. The analysis of the secondary flows here suggests that the same localization occurs in these poloxamer WLMs. Disturbances of particles in the low-shear-rate band of fluid were shown to propagate in the flow direction with a speed proportional to velocity of the high-shear-rate band fluid, which suggests that these secondary flows originate in the fluidized region. While this type of localized bulk instability in the high shear rate band is the most commonly observed, secondary flows and interface undulations could result from a purely interfacial instability [114–116], which may be more likely at smaller shear rates when the high-shear-rate band is thin [116].

Without flow visualization along the vorticity axis, we cannot definitely state which mechanism applies here. Nonetheless, at low shear rates, the high-shear rate band is so thin that the secondary flow driven by interfacial instabilities is more likely. Interfacial instabilities have been shown in flows of viscous liquids across an elastic solid in the Couette flow, a potential analogy for shear bands of these WLMs gels with a nonfluidized region. Interfacial waves are predicted to form in such systems beyond a critical strain [117,118]; complementary experimental works reported critical stresses for this instability that agreed with these theoretical predictions [119,120]. There, the mean flow of the viscous fluid was found to amplify interfacial perturbations; here, the flow of the high rate band region appears to drive the low-shear-rate band fluctuations, as suggested by the propagation speed of radial fluctuations in the flow direction (Table S3 [59]). However, significant stress oscillations accompanied this instability in the experiments of Eggert and Kumar [119]; here, only small stress fluctuations are observed at $\dot{\gamma} = 0.5\,\mathrm{s}^{-1}$. Interfacial instabilities have been predicted without significant stress fluctuation in flow simulations of viscoelastic WLMs using the diffusive Johnson Segalman (dJS) [115]. Given the combination of the yield stress and high elasticity of these WLM gels, more work is needed to understand the nature of these secondary flows, necessitating characterization along the vorticity axis.

F. Wall slip

Although wall slip has the potential to interact with elastic instabilities [33,40,91], here the increased turbidity of the high rate band prevents accurate tracking of particles at long times when secondary flows become significant (Fig. S23 [59]). Even at earlier times when particle motion high rate band can be captured, the impact of wall slip is difficult to characterize given the small width of the high shear rate band [Figs. 4(d)–4(f)]. At the lowest shear rate examined, $\dot{\gamma} = 0.02\,\mathrm{s}^{-1}$, discerning wall slip from a thin, high shear rate band of fluid is especially challenging as the band interface is only 1/20th of the gap width from the inner wall.

Interestingly, wall slip is least prevalent during flow reversal (Fig. 6). In contrast, flow reversal observed in Carbopol was associated with failure at the boundary and a large magnitude of wall slip [19]. This wall slip was attributed to a thin lubricating layer that subsequently fluidized the sample and, therefore, wall slip and fluidization were correlated. However, in these P234 WLM gels, the width of the fluidized region remains unchanged (Fig. S14 [59]) despite large variations in the slip velocity. Significant wall slip might have been expected here given the magnitude of the shear rate at the moving inner wall is greatest during flow reversal [Fig. 8(a)]. A previous study of CPyCl/NaSal WLMs found steady state wall slip scaled linearly with the shear rate in the high rate band [40], a trend that evidently does not extend to the transient process of shear band formation examined here, suggesting that wall slip exhibits complex dynamics during shear band formation that is possibly system- or geometry-dependent.

V. CONCLUSIONS

The formation and evolution of the heterogeneous flow were examined in a 15% wt poloxamer WLM gel via a combination of nonlinear rheology and particle tracking velocimetry. The combination of elasticity imparted by WLMs and

viscoelastic aging and yield stress leads to unique flow behaviors like wall slip and elastic instabilities. The most notable feature, the large elastic recoil and flow reversal during startup, is possible because of the large elasticity of the WLMs combined with a mechanism of heterogeneous flow formation similar to that seen in aging yield stress fluids. In this mechanism, the heterogeneous flow develops immediately following the maximum stress in the stress overshoot region. Particle tracking measurements during the startup flow on a broader set of materials that exhibit both a yield stress and substantial elasticity would validate the proposed flow reversal criteria. Such measurements on WLM gels with a range of rheological properties are of particular interest to determine whether the flow kinematics observed here are unique to this poloxamer system or occur more generally in this class of materials. In this regard, poloxamers are a promising class of surfactants, given the range of solution properties that can be accessed by varying the block composition and solution conditions.

ACKNOWLEDGMENTS

The authors acknowledge the support of the Institut Laue Langevin for providing the neutron research facilities used in this work. This material is based upon work supported by the National Science Foundation Graduate Research Fellowship under Grant No. 00074041. Additionally, this work was supported partially by the Research Experiences for Undergraduates (REU) Program and the University of Minnesota MRSEC through the National Science Foundation under Award Nos. DMR-2011401 and DMR-2244111. The authors thank the Anton Paar VIP program for the rheometer used in this work. The authors also thank Michael C. Burroughs at UC Santa Barbara for his generous advice and guidance on conducting particle tracking velocimetry measurements.

AUTHOR DECLARATIONS

Conflict of Interest

The authors have no conflicts to disclose.

REFERENCES

[1] Raghavan, S. R., and Y. Feng, "Wormlike micelles: Solutions, gels, or both?," in *Wormlike Micelles* (Royal Society of Chemistry, London, 2017), pp. 9–30.

[2] Raghavan, S. R., and E. W. Kaler, "Highly viscoelastic wormlike micellar solutions formed by cationic surfactants with long unsaturated tails," Langmuir **17**, 300–306 (2001).

[3] Chu, Z., and Y. Feng, "Amidosulfobetaine surfactant gels with shear banding transitions," Soft Matter **6**, 6065–6067 (2010).

[4] Gupta, R., R. Mitishita, I. A. Frigaard, and G. J. Elfring, "Rheology of wormlike micellar gels formed by long-chained zwitterionic surfactants," J. Rheol. **65**, 1065–1080 (2021).

[5] Gyr, A., and H.-W. Bewersdorff, *Drag Reduction of Turbulent Flows by Additives* (Springer Science & Business Media, New York, 2013), Vol. 32.

[6] Calabrese, M. A., and N. J. Wagner, New insights from rheo-small-angle neutron scattering, in *Wormlike Micelles: Systems, Characterisation and Applications* (RSC Publishing, London, 2017), Chap. 8, pp. 193–235.

[7] Manneville, S., A. Colin, G. Waton, and F. Schosseler, "Wall slip, shear banding, and instability in the flow of a triblock copolymer micellar solution," Phys. Rev. E **75**, 061502 (2007).

[8] Olmsted, P. D., "Perspectives on shear banding in complex fluids," Rheol. Acta **47**, 283–300 (2008).

[9] Fielding, S. M., "Complex dynamics of shear banded flows," Soft Matter **3**, 1262–1279 (2007).

[10] Cates, M., "Nonlinear viscoelasticity of wormlike micelles (and other reversibly breakable polymers)," J. Phys. Chem. **94**, 371–375 (1990).

[11] Hu, Y. T., and A. Lips, "Kinetics and mechanism of shear banding in an entangled micellar solution," J. Rheol. **49**, 1001–1027 (2005).

[12] Hemingway, E. J., and S. M. Fielding, "Edge-induced shear banding in entangled polymeric fluids," Phys. Rev. Lett. **120**, 138002 (2018).

[13] Hu, Y. T., "Steady-state shear banding in entangled polymers?," J. Rheol. **54**, 1307–1323 (2010).

[14] Helgeson, M. E., L. Porcar, C. Lopez-Barron, and N. J. Wagner, "Direct observation of flow-concentration coupling in a shear-banding fluid," Phys. Rev. Lett. **105**, 084501 (2010).

[15] Fielding, S. M., and P. D. Olmsted, "Flow phase diagrams for concentration-coupled shear banding," Eur. Phys. J. E **11**, 65–83 (2003).

[16] Divoux, T., M. A. Fardin, S. Manneville, and S. Lerouge, "Shear banding of complex fluids," Annu. Rev. Fluid Mech. **48**, 81–103 (2016).

[17] Ovarlez, G., S. Rodts, X. Chateau, and P. Coussot, "Phenomenology and physical origin of shear localization and shear banding in complex fluids," Rheol. Acta **48**, 831–844 (2009).

[18] Moorcroft, R. L., and S. M. Fielding, "Shear banding in time-dependent flows of polymers and wormlike micelles," J. Rheol. **58**, 103–147 (2014).

[19] Divoux, T., D. Tamarii, C. Barentin, and S. Manneville, "Transient shear banding in a simple yield stress fluid," Phys. Rev. Lett. **104**, 208301 (2010).

[20] Martin, J. D., and Y. T. Hu, "Transient and steady-state shear banding in aging soft glassy materials," Soft Matter **8**, 6940–6949 (2012).

[21] Kurokawa, A., V. Vidal, K. Kurita, T. Divoux, and S. Manneville, "Avalanche-like fluidization of a non-brownian particle gel," Soft Matter **11**, 9026–9037 (2015).

[22] Hu, Y. T., C. Palla, and A. Lips, "Comparison between shear banding and shear thinning in entangled micellar solutions," J. Rheol. **52**, 379–400 (2008).

[23] Miller, E., and J. P. Rothstein, "Transient evolution of shear-banding wormlike micellar solutions," J. Non-Newtonian Fluid Mech. **143**, 22–37 (2007).

[24] Fardin, M.-A., B. Lasne, O. Cardoso, G. Grégoire, M. Argentina, J.-P. Decruppe, and S. Lerouge, "Taylor-like vortices in shear-banding flow of giant micelles," Phys. Rev. Lett. **103**, 028302 (2009).

[25] Calabrese, M. A., S. A. Rogers, R. P. Murphy, and N. J. Wagner, "The rheology and microstructure of branched micelles under shear," J. Rheol. **59**, 1299–1328 (2015).

[26] Helgeson, M. E., P. A. Vasquez, E. W. Kaler, and N. J. Wagner, "Rheology and spatially resolved structure of cetyltrimethylammonium bromide wormlike micelles through the shear banding transition," J. Rheol. **53**, 727–756 (2009).

[27] López-Barrón, C. R., A. K. Gurnon, A. P. Eberle, L. Porcar, and N. J. Wagner, "Microstructural evolution of a model, shear-banding micellar solution during shear startup and cessation," Phys. Rev. E **89**, 042301 (2014).

[28] Calabrese, M. A., S. A. Rogers, L. Porcar, and N. J. Wagner, "Understanding steady and dynamic shear banding in a model wormlike micellar solution," J. Rheol. **60**, 1001–1017 (2016).
[29] Berret, J.-F., "Transient rheology of wormlike micelles," Langmuir **13**, 2227–2234 (1997).
[30] Divoux, T., C. Barentin, and S. Manneville, "Stress overshoot in a simple yield stress fluid: An extensive study combining rheology and velocimetry," Soft Matter **7**, 9335–9349 (2011).
[31] Radulescu, O., P. Olmsted, J. Decruppe, S. Lerouge, J.-F. Berret, and G. Porte, "Time scales in shear banding of wormlike micelles," Europhys. Lett. **62**, 230–236 (2003).
[32] Divoux, T., D. Tamarii, C. Barentin, S. Teitel, and S. Manneville, "Yielding dynamics of a herschel–bulkley fluid: A critical-like fluidization behaviour," Soft Matter **8**, 4151–4164 (2012).
[33] Bécu, L., S. Manneville, and A. Colin, "Spatiotemporal dynamics of wormlike micelles under shear," Phys. Rev. Lett. **93**, 018301 (2004).
[34] Douglass, B. S., R. H. Colby, L. A. Madsen, and P. T. Callaghan, "Rheo-NMR of wormlike micelles formed from nonionic pluronic surfactants," Macromolecules **41**, 804–814 (2008).
[35] Calabrese, M. A., Ph.D. thesis, University of Delaware, 2017.
[36] Adams, J., S. Fielding, and P. Olmsted, "The interplay between boundary conditions and flow geometries in shear banding: Hysteresis, band configurations, and surface transitions," J. Non-Newtonian Fluid Mech. **151**, 101–118 (2008).
[37] Bécu, L., D. Anache, S. Manneville, and A. Colin, "Evidence for three-dimensional unstable flows in shear-banding wormlike micelles," Phys. Rev. E **76**, 011503 (2007).
[38] Fardin, M.-A., L. Casanellas, B. Saint-Michel, S. Manneville, and S. Lerouge, "Shear-banding in wormlike micelles: Beware of elastic instabilities," J. Rheol. **60**, 917–926 (2016).
[39] Lerouge, S., M.-A. Fardin, M. Argentina, G. Grégoire, and O. Cardoso, "Interface dynamics in shear-banding flow of giant micelles," Soft Matter **4**, 1808–1819 (2008).
[40] Fardin, M., T. Divoux, M. Guedeau-Boudeville, I. Buchet-Maulien, J. Browaeys, G. McKinley, S. Manneville, and S. Lerouge, "Shear-banding in surfactant wormlike micelles: Elastic instabilities and wall slip," Soft Matter **8**, 2535–2553 (2012).
[41] Briole, A., L. Casanellas, M.-A. Fardin, C. Py, O. Cardoso, J. Browaeys, and S. Lerouge, "Shear-banding fluid (s) under time-dependent shear flows. part I: Spatiotemporal dynamics," J. Rheol. **65**, 1187–1200 (2021).
[42] Fardin, M.-A., D. Lopez, J. Croso, G. Grégoire, O. Cardoso, G. McKinley, and S. Lerouge, "Elastic turbulence in shear banding wormlike micelles," Phys. Rev. Lett. **104**, 178303 (2010).
[43] Beaumont, J., N. Louvet, T. Divoux, M.-A. Fardin, H. Bodiguel, S. Lerouge, S. Manneville, and A. Colin, "Turbulent flows in highly elastic wormlike micelles," Soft Matter **9**, 735–749 (2013).
[44] Mohammadigoushki, H., A. Dalili, L. Zhou, and P. Cook, "Transient evolution of flow profiles in a shear banding wormlike micellar solution: Experimental results and a comparison with the vcm model," Soft Matter **15**, 5483–5494 (2019).
[45] Ravindranath, S., S.-Q. Wang, M. Olechnowicz, and R. P. Quirk, "Banding in simple steady shear of entangled polymer solutions," Macromolecules **41**, 2663–2670 (2008).
[46] Hu, Y. T., L. Wilen, A. Philips, and A. Lips, "Is the constitutive relation for entangled polymers monotonic?," J. Rheol. **51**, 275–295 (2007).
[47] Erk, K. A., J. D. Martin, Y. T. Hu, and K. R. Shull, "Extreme strain localization and sliding friction in physically associating polymer gels," Langmuir **28**, 4472–4478 (2012).
[48] Rassolov, P., and H. Mohammadigoushki, "Effects of elasticity and flow ramp up on kinetics of shear banding flow formation in wormlike micellar fluids," J. Rheol. **64**, 1161–1177 (2020).
[49] Rassolov, P., and H. Mohammadigoushki, "Role of micellar entanglements on kinetics of shear banding flow formation," J. Rheol. **67**, 169–181 (2023).
[50] Zhou, L., G. H. McKinley, and L. P. Cook, "Wormlike micellar solutions: III. VCM model predictions in steady and transient shearing flows," J. Non-Newtonian Fluid Mech. **211**, 70–83 (2014).
[51] Germann, N., L. Cook, and A. Beris, "Investigation of the inhomogeneous shear flow of a wormlike micellar solution using a thermodynamically consistent model," J. Non-Newtonian Fluid Mech. **207**, 21–31 (2014).
[52] Germann, N., A. Kate Gurnon, L. Zhou, L. Pamela Cook, A. N. Beris, and N. J. Wagner, "Validation of constitutive modeling of shear banding, threadlike wormlike micellar fluids," J. Rheol. **60**, 983–999 (2016).
[53] Kumar, R., G. C. Kalur, L. Ziserman, D. Danino, and S. R. Raghavan, "Wormlike micelles of a c22-tailed zwitterionic betaine surfactant: From viscoelastic solutions to elastic gels," Langmuir **23**, 12849–12856 (2007).
[54] McCauley, P., S. Kumar, and M. Calabrese, "Criteria governing rod formation and growth in nonionic polymer wormlike micelles," Langmuir **37**, 11676–11687 (2021).
[55] Waton, G., B. Michels, A. Steyer, and F. Schosseler, "Shear-induced demixing and shear-banding instabilities in dilute triblock copolymer solutions," Macromolecules **37**, 2313–2321 (2004).
[56] Rogers, S. A., M. A. Calabrese, and N. J. Wagner, "Rheology of branched wormlike micelles," Curr. Opin. Colloid Interface Sci. **19**, 530–535 (2014).
[57] Ahmed, T., and K. Aramaki, "Wormlike micelles in poly (oxyethylene) surfactant solution: Growth control through hydrophilic-group size variation," J. Colloid Interface Sci. **327**, 180–185 (2008).
[58] Ahmed, T., and K. Aramaki, "Temperature sensitivity of wormlike micelles in poly (oxyethylene) surfactant solution: Importance of hydrophilic-group size," J. Colloid Interface Sci. **336**, 335–344 (2009).
[59] See the supplementary material at https://www.scitation.org/doi/suppl/10.1122/8.0000535 for additional aging measurements at 39 °C, consideration of wormlike micelle branching, controlled-stress and controlled-shear-rate measurements used to construct the flow curve, supplemental flow curve measurements, estimates of the WLM parameters, a full description of the small-angle-neutron scattering micelle model and data fitting, high-shear-rate PTV results, replicate PTV results at low shear rates, characterization of sample fracture, characterization of the shear band properties including high shear rate data, PTV using a smaller gap concentric cylinder geometry, characterization of secondary flows at additional shear rates, flow-SANS measurements in step-shear and startup measurements, and supplemental videos of flow reversal, band interface undulations, sample fracture, and high shear rate instabilities.
[60] López-Barrón, C. R., and N. J. Wagner, "Solvent isotope effect on the microstructure and rheology of cationic worm-like micelles near the isotropic-nematic transition," Soft Matter **7**, 10856–10863 (2011).
[61] Fardin, M., T. Ober, V. Grenard, T. Divoux, S. Manneville, G. McKinley, and S. Lerouge, "Interplay between elastic instabilities and shear-banding: Three categories of Taylor-Couette flows and beyond," Soft Matter **8**, 10072–10089 (2012).
[62] Rassolov, P., A. Scigliani, and H. Mohammadigoushki, "Kinetics of shear banding flow formation in linear and branched wormlike micelles," Soft Matter **18**, 6079–6093 (2022).

[63] Denkova, A., E. Mendes, and M. Coppens, "Effects of salts and ethanol on the population and morphology of triblock copolymer micelles in solution," J. Phys. Chem. B **112**, 793–801 (2008).
[64] Denkova, A., E. Mendes, and M.-O. Coppens, "Rheology of worm-like micelles composed of tri-block copolymer in the limit of slow dynamics," J. Rheol. **53**, 1087–1100 (2009).
[65] Linse, P., "Phase behavior of poly (ethylene oxide)-poly (propylene oxide) block copolymers in aqueous solution," J. Phys. Chem. **97**, 13896–13902 (1993).
[66] Joshi, Y. M., and G. Petekidis, "Yield stress fluids and ageing," Rheol. Acta **57**, 521–549 (2018).
[67] Larson, R. G., and Y. Wei, "A review of thixotropy and its rheological modeling," J. Rheol. **63**, 477–501 (2019).
[68] Allan, D. B., T. Caswell, N. C. Keim, C. M. van der Wel, and R. W. Verweij, "soft-matter/trackpy: Trackpy v0.5.0." (2021).
[69] Crocker, J. C., and D. G. Grier, "Methods of digital video microscopy for colloidal studies," J. Colloid Interface Sci. **179**, 298–310 (1996).
[70] Calabrese, M. A., and L. Porcar, *Precise Determination of Concentration Gradient in Shear Banding Wormlike Micelle Solutions* (Institut Laue Langevin (ILL), Grenoble, 2017).
[71] Pedersen, J. S., and M. C. Gerstenberg, "The structure of p85 pluronic block copolymer micelles determined by small-angle neutron scattering," Colloids Surf. A **213**, 175–187 (2003).
[72] Pedersen, J. S., "Form factors of block copolymer micelles with spherical, ellipsoidal and cylindrical cores," J. Appl. Crystallogr. **33**, 637–640 (2000).
[73] Pedersen, J. S., "Structure factors effects in small-angle scattering from block copolymer micelles and star polymers," J. Chem. Phys. **114**, 2839–2846 (2001).
[74] Tan, G., W. Zou, M. Weaver, and R. G. Larson, "Determining thread-like micelle lengths from rheometry," J. Rheol. **65**, 59–71 (2021).
[75] Gurnon, A. K., C. R. Lopez-Barron, A. P. Eberle, L. Porcar, and N. J. Wagner, "Spatiotemporal stress and structure evolution in dynamically sheared polymer-like micellar solutions," Soft Matter **10**, 2889–2898 (2014).
[76] Bonnecaze, R., and J. Brady, "Yield stresses in electrorheological fluids," J. Rheol. **36**, 73–115 (1992).
[77] Pham, K., G. Petekidis, D. Vlassopoulos, S. Egelhaaf, W. Poon, and P. Pusey, "Yielding behavior of repulsion-and attraction-dominated colloidal glasses," J. Rheol. **52**, 649–676 (2008).
[78] Ziegelbaur, R., and J. Caruthers, "Rheological properties of poly (dimethylsiloxane) filled with fumed silica: I. hysteresis behaviour," J. Non-Newtonian Fluid Mech. **17**, 45–68 (1985).
[79] Divoux, T., V. Grenard, and S. Manneville, "Rheological hysteresis in soft glassy materials," Phys. Rev. Lett. **110**, 018304 (2013).
[80] Puisto, A., M. Mohtaschemi, M. J. Alava, and X. Illa, "Dynamic hysteresis in the rheology of complex fluids," Phys. Rev. E **91**, 042314 (2015).
[81] Barnes, H. A., "A review of the slip (wall depletion) of polymer solutions, emulsions and particle suspensions in viscometers: Its cause, character, and cure," J. Non-Newtonian Fluid Mech. **56**, 221–251 (1995).
[82] Lettinga, M. P., and S. Manneville, "Competition between shear banding and wall slip in wormlike micelles," Phys. Rev. Lett. **103**, 248302 (2009).
[83] Kalyon, D. M., P. Yaras, B. Aral, and U. Yilmazer, "Rheological behavior of a concentrated suspension: A solid rocket fuel simulant," J. Rheol. **37**, 35–53 (1993).
[84] Marchesini, F. H., M. F. Naccache, A. Abdu, A. A. Alicke, and P. R. de Souza Mendes, "Rheological characterization of yield-stress materials: Flow pattern and apparent wall slip," Appl. Rheol. **25**, 53883 (2015).
[85] Bertola, V., F. Bertrand, H. Tabuteau, D. Bonn, and P. Coussot, "Wall slip and yielding in pasty materials," J. Rheol. **47**, 1211–1226 (2003).
[86] Coussot, P., J. Raynaud, F. Bertrand, P. Moucheront, J. Guilbaud, H. Huynh, S. Jarny, and D. Lesueur, "Coexistence of liquid and solid phases in flowing soft-glassy materials," Phys. Rev. Lett. **88**, 218301 (2002).
[87] Moorcroft, R. L., M. E. Cates, and S. M. Fielding, "Age-dependent transient shear banding in soft glasses," Phys. Rev. Lett. **106**, 055502 (2011).
[88] Schweizer, T., "Shear banding during nonlinear creep with a solution of monodisperse polystyrene," Rheol. Acta **46**, 629–637 (2007).
[89] Hemingway, E. J., H. Kusumaatmaja, and S. M. Fielding, "Edge fracture in complex fluids," Phys. Rev. Lett. **119**, 028006 (2017).
[90] Lettinga, M., and J. Dhont, "Non-equilibrium phase behaviour of rod-like viruses under shear flow," J. Phys.-Condens. Mat. **16**, S3929–S3939 (2004).
[91] Feindel, K. W., and P. T. Callaghan, "Anomalous shear banding: Multidimensional dynamics under fluctuating slip conditions," Rheol. Acta **49**, 1003–1013 (2010).
[92] Salmon, J.-B., A. Colin, S. Manneville, and F. Molino, "Velocity profiles in shear-banding wormlike micelles," Phys. Rev. Lett. **90**, 228303 (2003).
[93] Fardin, M.-A., and S. Lerouge, "Instabilities in wormlike micelle systems," Eur. Phys. J. E **35**, 1–29 (2012).
[94] Decruppe, J., O. Greffier, S. Manneville, and S. Lerouge, "Local velocity measurements in heterogeneous and time-dependent flows of a micellar solution," Phys. Rev. E **73**, 061509 (2006).
[95] Geri, M., B. Saint-Michel, T. Divoux, G. H. McKinley, and S. Manneville, "A generalized lever rule for shear banding of yield stress fluids," arXiv:2111.08623 (2021).
[96] Cheng, P., M. C. Burroughs, L. G. Leal, and M. E. Helgeson, "Distinguishing shear banding from shear thinning in flows with a shear stress gradient," Rheol. Acta **56**, 1007–1032 (2017).
[97] Fardin, M.-A., T. Ober, C. Gay, G. Grégoire, G. McKinley, and S. Lerouge, "Criterion for purely elastic Taylor-Couette instability in the flows of shear-banding fluids," Europhys. Lett. **96**, 44004 (2011).
[98] Da Cruz, F., F. Chevoir, D. Bonn, and P. Coussot, "Viscosity bifurcation in granular materials, foams, and emulsions," Phys. Rev. E **66**, 051305 (2002).
[99] Malkin, A., V. Kulichikhin, and S. Ilyin, "A modern look on yield stress fluids," Rheol. Acta **56**, 177–188 (2017).
[100] Hyun, K., M. Wilhelm, C. O. Klein, K. S. Cho, J. G. Nam, K. H. Ahn, S. J. Lee, R. H. Ewoldt, and G. H. McKinley, "A review of nonlinear oscillatory shear tests: Analysis and application of large amplitude oscillatory shear (LAOS)," Prog. Polym. Sci. **36**, 1697–1753 (2011).
[101] Ovarlez, G., F. Bertrand, and S. Rodts, "Local determination of the constitutive law of a dense suspension of noncolloidal particles through magnetic resonance imaging," J. Rheol. **50**, 259–292 (2006).
[102] Brox, T. I., B. Douglass, P. Galvosas, and J. R. Brown, "Observations of the influence of Taylor-Couette geometry on the onset of shear-banding in surfactant wormlike micelles," J. Rheol. **60**, 973–982 (2016).
[103] Coussot, P., L. Tocquer, C. Lanos, and G. Ovarlez, "Macroscopic versus local rheology of yield stress fluids," J. Non-Newtonian Fluid Mech. **158**, 85–90 (2009).
[104] Dimitriou, C. J., and G. H. McKinley, "A comprehensive constitutive law for waxy crude oil: A thixotropic yield stress fluid," Soft Matter **10**, 6619–6644 (2014).

[105] Martens, K., L. Bocquet, and J.-L. Barrat, "Spontaneous formation of permanent shear bands in a mesoscopic model of flowing disordered matter," Soft Matter **8**, 4197–4205 (2012).

[106] Besseling, R., L. Isa, P. Ballesta, G. Petekidis, M. Cates, and W. Poon, "Shear banding and flow-concentration coupling in colloidal glasses," Phys. Rev. Lett. **105**, 268301 (2010).

[107] Shereda, L. T., R. G. Larson, and M. J. Solomon, "Shear banding in crystallizing colloidal suspensions," Korea-Aust. Rheol. J. **22**, 309–316 (2010).

[108] Divoux, T., C. Barentin, and S. Manneville, "From stress-induced fluidization processes to herschel-bulkley behaviour in simple yield stress fluids," Soft Matter **7**, 8409–8418 (2011).

[109] Bonn, D., M. M. Denn, L. Berthier, T. Divoux, and S. Manneville, "Yield stress materials in soft condensed matter," Rev. Mod. Phys. **89**, 035005 (2017).

[110] Benzi, R., T. Divoux, C. Barentin, S. Manneville, M. Sbragaglia, and F. Toschi, "Stress overshoots in simple yield stress fluids," Phys. Rev. Lett. **127**, 148003 (2021).

[111] Taylor, G. I., "VIII. Stability of a viscous liquid contained between two rotating cylinders," Philos. Trans. Roy. Soc. London Ser. A **223**, 289–343 (1923).

[112] Larson, R. G., "Instabilities in viscoelastic flows," Rheol. Acta **31**, 213–263 (1992).

[113] Fardin, M., C. Perge, N. Taberlet, and S. Manneville, "Flow-induced structures versus flow instabilities," Phys. Rev. E **89**, 011001 (2014).

[114] Fielding, S. M., "Linear instability of planar shear banded flow," Phys. Rev. Lett. **95**, 134501 (2005).

[115] Fielding, S., and P. Olmsted, "Nonlinear dynamics of an interface between shear bands," Phys. Rev. Lett. **96**, 104502 (2006).

[116] Nicolas, A., and A. Morozov, "Nonaxisymmetric instability of shear-banded Taylor-Couette flow," Phys. Rev. Lett. **108**, 088302 (2012).

[117] Gkanis, V., and S. Kumar, "Instability of creeping Couette flow past a neo-Hookean solid," Phys. Fluids **15**, 2864–2871 (2003).

[118] Kumaran, V., G. Fredrickson, and P. Pincus, "Flow induced instability of the interface between a fluid and a gel at low reynolds number," J. Phys. II **4**, 893–911 (1994).

[119] Eggert, M. D., and S. Kumar, "Observations of instability, hysteresis, and oscillation in low-reynolds-number flow past polymer gels," J. Colloid Interface Sci. **278**, 234–242 (2004).

[120] Kumaran, V., and R. Muralikrishnan, "Spontaneous growth of fluctuations in the viscous flow of a fluid past a soft interface," Phys. Rev. Lett. **84**, 3310–3313 (2000).